Recognizing Incipient Epizootic Shell Disease Lesions in the Carapace of the American Lobster, *Homarus americanus* H. Milne Edwards 1837

Running title: Recognizing Incipient Epizootic Shell Disease in American Lobster

Joseph G. Kunkel*[1,2], Melissa Rosa[2] , Brian Tarbox[3],
Sabine Hild[4], Michael J. Jercinovic[5], Ali N. Bahadur[6]

[1] Biology, University of Massachusetts Amherst, Massachusetts 01003
[2] Marine Sciences, University of New England, Biddeford, Maine 04005
[3] Marines Sciences, Southern Maine Community College, South Portland, Maine 04106
[4] Polymer Science Institute, Johannes Kepler University, Linz, Austria A-4040
[5] Geosciences, University of Massachusetts Amherst, Massachusetts 01003
[6] Bruker BioSpin Corp., Billerica, Massachusetts 01821
* Corresponding author email: <joe@bio.umass.edu>, phone (413) 335-6017

ABSTRACT: Causal factors leading to Epizootic Shell Disease (ESD) lesions in American Lobster, *H. americanus*, are not well understood. We explore the structural and physiological bases for development of ESD from preclinical stages invisible to unaided eye to early visible stages. We present a lobster shell model which develops structural functional vulnerability and suggests plausible routes to ESD. Medallions of carapace cuticle are obtained from carapace fixed with protocols to minimize movement of mineral and macromolecular components. Rapid processing of medallions is used to encourage large sample sizes compatible with environmental surveys. One- and two-dimensional analytic maps of polished sections of the cuticle, obtained with an Electron Microprobe, describe the composite mineral and polymeric structures. MicroRaman Spectroscopy was used to identify bond properties of phosphates and carbonates as well as signatures of organic structures. The frequency and properties of structures identified can be monitored through the lobster molting cycle using a high throughput application of micro-Computed Tomography (μCT). We observed density differences in the calcite layer, exocuticle and endocuticle and the frequency and structure of $CaCO_3$ structures in the endocuticle and membranous layer of carapace cuticle during chosen stages of the molting cycle. The correlative microscopy and μCT of shell structures allows an improved understanding of the lobster cuticle structure. Detailed structural differences quantified through development and under different environmental conditions can provide insight into causes and vulnerabilities associated with ESD.

INTRODUCTION

American lobster populations experienced increased and variable incidence of Epizootic Shell Disease (ESD) (Smolowitz et al. 2005, Glenn and Pugh 2006) starting in 1978 (Castro et al. 2006, 2012). The basis of observed localized and variable ESD rates is not clear. Several causal factors have been suggested (Shields et al. 2012) including residual pollution from the 1996 North Cape oil spill (NOAA 2009), an association with industrial compounds such as alkylphenols (Laufer et al. 2012) and rising

43 mean temperatures south of Cape Cod (Tlusty et al. 2007). Irrespective of remediation efforts and
44 causal factors the lobster population south of Cape Cod has effectively collapsed leaving behind a
45 remnant of the earlier fishery (Mandel 2016).

46 However, recent record harvests of American lobster have been recorded in both American and
47 Canadian waters correlated with rising temperatures in the Gulf of Maine (University of Maine 2017)
48 and lowered populations of top predators (Steneck and Wahle 2013). The phenomenon of global
49 warming is being imposed on arrays of populations of species of Northern Hemisphere organisms that
50 have responded with shifts northward (Perry et al. 2005). However for the American lobster, moving
51 northward was correlated with and included the population collapse south of Cape Cod, which was
52 correlated with, and some think caused by, ESD (Castro et al. 2012). The ESD based decline of lobster
53 populations south of Cape Cod is argued, mainly logically, on the observation that females carrying
54 eggs delay their molting cycle giving shell disease lesions longer times to compromise the female
55 carapace shell, and in addition, egged lobsters with ESD are observed to fail to survive molting at
56 higher frequency than non-ESD egged females (Castro et al. 2012). While ESD frequency has
57 increased markedly in the Gulf of Maine from historically low levels of 1 per thousand, the observation
58 now is that the Gulf of Maine population remains relatively healthy with an ESD incidence below 1
59 percent overall (Maine DMR 2016). However, in the southernmost Lobster Management Zones E, F
60 and G, the level of ESD has risen to 2-2.5% as reported 2012-2016 (Maine DMR 2016). There are also
61 independent reports of hot spots of ESD found in particular Gulf of Maine locations where up to 1 in 5
62 lobsters are found to have ESD at its peak development seen in late fall and early spring similar to the
63 phenomenon of localized higher frequency observed in Buzzards Bay, MA (Stevens 2009). There is
64 some urgency for practical as well as theoretical reasons in being able to detect shell disease at its
65 earliest stages and to predict areas of imminent higher frequency. Until the earliest signs of shell

disease can be discerned the precise causes will be hard to identify.

The main objective of this study is to develop a rapid high-throughput approach to evaluating lobster carapace architecture. We focus on structural and functional aspects of the shell in order to understand their potential for predicting the onset of ESD in Gulf of Maine populations. The dorsal carapace, the typical anatomical location where ESD is first seen, was chosen as the principle structure to be studied. An initial objective is recognizing the earliest stages of ESD but, more important, being able to recognize lobster vulnerability that will predict that ESD will develop. Our model population is in an area just outside the major islands of Casco Bay, Maine, which in our experience has in the past several years been a hotspot of ESD. In any location, harvesting a population sometime prior to peak ESD development could yield a substantially healthier crop that would be less marketable later in the season. Strategies for bringing product to market earlier or avoiding impoundment, during which shell disease might develop, could lessen the economic impact of ESD in particular seasons if the potential incidence could be predicted. We establish here the chemical and physical basis for understanding the structure of the lobster carapace cuticle and, based on that structure, demonstrate a rapid approach to high throughput data collection and analysis for prediction of a population's future vulnerability to ESD.

METHODS

Animals

American lobster non-shell diseased individuals were regularly collected from an area with low prevalence of ESD, inner Casco Bay (Maine DMR 2016) in region F. Though these inner Casco Bay animals typically did not display ESD we were reluctant to identify them as totally ESD free given the reports of approximate 2.5% ESD prevalence in region F. ESD infected American lobster individuals

were regularly obtained from traps at locations outside the major islands of Casco Bay, which from past years experience we describe as having a high incidence of ESD. Each year trap locations changed somewhat but a typical year trap placement in 2013 is provided in map form as supplementary Fig. S1 in which trap locations TB01-TB06 are considered 'inner Casco Bay' and TB09-TB19 are considered 'outer Casco Bay'. Prior to 2017 in seasons 2014 to 2016 the number of ESD lobsters collected by us in inner Casco Bay was non-existent from 40 traps hauled once per 4 day soak throughout the summer and into thhe fall. In outer Casco Bay traps, ESD reached as high as 1 in 5 and could be consistently depended on to provide well established ESD in part of the carapace, but include areas of carapace free of ESD or with small ESD lesions. Sub-clinical lesions were sought in lobsters which exhibited well defined small lesions outside an area of more extensive existing lesions. This was based on prior experience of housing early-recognized clinical ESD animals and observing that new lesions developed in areas outside the current lesions that would have been described as sub-clinical or ESD-free. Outer Casco Bay trapped animals provided us with clinically identifiable ESD lobsters, such as the specimens seen in Fig. 1, as well as ESD-lesion-free animals that we describe as members of a vulnerable population. Lobsters were maintained in the UNE Marine Scince Center life table with running fresh sea water averaging approximately 15ºC during the late spring and processed for sampling within days of collection unless they were maintained in the life table for later sampling. Maintained animals were fed twice weekly with herring. Animals were euthanized at the end of the experiment by freezing. The four medallions from two ESD animals described here (Table I) were compared to medallions from a historically ESD free population (Kunkel et al. 2016) from outer Georges Bank which were sampled at sea using the plunge freeze aparatus described below. Staging of the lobster molting cycle is taken from (Waddy et al. 1995).

Tissue Preparation

Medallions of cuticle were obtained using a drill press (Micro-Mark MicroLux® Benchtop Variable Speed Mini Drill Press) with a 7 mm diamond coring bit which produced 6 mm medallions of cuticle. All medallions were prepared as described (Kunkel et al. 2016). Specifically, medallions were plunge-freeze fixed in a -40ºC acetone bath with BioBeads to scavenge any released water and gradually returned to room temperature over a 24 hour period with several changes of cold anhydrous acetone. In the absence of water, the acetone was allowed to evaporate leaving a dry medallion. Some medallions were affixed to 26 mm plastic blanks, ground with carborundum paper to desired observation level and polished with diamond polish (transitioning from 6 μm to 0.25 μm) to reveal planar views of cuticle structures as a polished face.

Data Collection

Selected areas of diamond polished surfaces of lobster cuticle (Kunkel et al. 2012) and standards were submitted to both electron microprobe (EMP, Cameca SX-50 and SX-100-Ultrachron, μass Geosciences Microprobe Facility) and micro-Raman spectrometry (Horibe Jobin Yvon Aramis, JKU Linz AT, Polymer Science Institute). A limited number of area integral spectra were collected with the Thermo-Fisher Scientific DXR Raman Microscope.

Seven medallions of lobster cuticle were submitted to the Skyscan1272 (Bruker, MicroCT, Kontich, Belgium) for voxel data collection, three ESD free medallions described in Kunkel and coworkers (2016, Table S1) and an additional four ESD associated medallions added here Table 1. The collection of μCT voxel data at 8 or 16 bit density resolution from the 6 mm medallions required substantial memory as indicated by the tabulated file sizes and computation power. The analytic software AnalyzePro (AnalyzeDirect, Inc., Overland Park, KS, 66085), ImageJ

(https://imagej.nih.gov/ij/) and R software (https://www.r-project.org/) required substantial memory and computation power and depending on protocols may access multiple cores when available. A MacBookPro with 4 cores and 16 Gb of memory was used to do post-data-collection analytic computations. In many cases data sets needed to be divided into Regions of Interest (ROI) to facilitate the analysis. When rotation of the data was necessary, DataViewer software (freely available from hardware manufacturers, e.g. Bruker) was used to subset, rotate and save data to a new stack of 8 or 16 bit voxel slices in a new orientation. When rotation was not necessary, ImageJ was used to load desired voxel slices and crop them to a desired ROI and saved as a stack with the same resolution or reduced resolution using ImageJ library functions.

Matrices of multivariate chemical composition data were collected from the Cameca-100 Ultrachron Electron Microprobe as raster arrays at 0.3 μm spacing (Kunkel and Jercinovic, 2012) and by raster collection of 2800 element μm^{-1} spectra by the Aramis Raman spectrometer at typical 2 μm array spacing from 0.25 μm diamond polished sample surfaces. The multivariate data was processed by matrix algebra in R which allowed using libraries that access multiple cores of the computer for operations that could use parallel processing. Principle Component Analysis was accomplished via singular value decomposition (svd) (Golub and Reinsch 1970) using the R base library svd function. Cluster analysis was performed on multivariate data using the k-means cluster function, kmeans, from the R stats library. PhotoStitcher (Maxim Gapchenko, iTunes) software was used to create montages of overlapping macro images of shell surface taken with a Zoomscope (Applicable Electronics, Cape Cod, MA) on a vibration suppression table with digital camera (IDS Imaging Development) using a translation stage (MicroMark, The MicroLux® X-Y Table) to position and move the specimen.

Data Collection Strategy

μCT reports 3-dimensional arrays of voxel density (Bruker 2015) for lobster cuticle. The voxel

155 slices from discrete volumes of cuticle can be analyzed slice by slice or as integrated volumes via
156 analytic software. The large amount of voxel density data collected, Kunkel and coworkers (2016 Table
157 S1) and reported here Table 1, can provide insights into the coordinated structure beyond the limits of
158 slices. Of particular interest to this study was vulnerable carapace surface structures: the epicuticular
159 calcite layer and its intersection with the carbonate apatite organule canals, interruption of either of
160 which could produce vulnerable targets for microorganisms. Additional interest is focused on
161 underlying structures such as the trabecular-exocuticle which supports the integrity of the surface
162 calcite and canal structures (Kunkel et al. 2016).

163 A potentially high-throughput μCT protocol for lobsters was designed to study the carapace
164 cuticle of a select number of lobster specimens, Table 1 and (Kunkel etal. 2016, Table S1). The
165 samples were chosen to provide contrasts of potential targets for advanced understanding of the role of
166 cuticle structure in vulnerability to ESD and to allow early detection. In this study, the seven
167 medallions of lobster cuticle were scanned at various resolutions (0.5, 1, 2.5 and 5 μm). Of the ESD
168 associated medallions, six were from lobster carapaces from 2 of potentially 4 sample categories
169 presented in Table 1. Three medallions were collected from a single late-intermolt (C4), lobster with
170 advancing ESD (Fig 1B), one from the dorsum of the large chela (with an ESD lesion) and two from
171 the carapace, one carapace medallion with a visible small lesion and another from adjacent carapace
172 sub-clinically lesion-free. A second ESD lobster was observed to molt to be sub-clinically free of ESD
173 and a medallion sampled one week post molting. Three medallions from clinically-lesion-free lobsters
174 at intermolt (C4) were obtained from control non-diseased lobster populations i.e. the outer edge of
175 Georges Bank (Kunkel et al. 2016).

176 One provisional strategy to recognize incipient ESD lesions is to extrapolate back to the earliest
177 ESD lesions recognizable by the naked eye and characterize their development and additionally look in

the sampled neighborhood for sub-clinical lesions using the high resolution and volume sampling of μCT. To do that we typically took the carapace, e.g. supplementary macro image Fig S2A, of a clinically ESD infected individual and looked on the periphery of its well developed ESD lesions with light microscopy shown in Fig 1A, to see smaller lesions that, from past experience, will develop into larger ESD lesions. Using the high-ESD-incidence population lobsters in outer Casco Bay we selected an individual stage C4 lobster (Fig 1B) in which an approximate 500 μm lesion was identified and included in a carapace medallion, Ha4, and another medallion free of LM visible lesions, Ha5, was collected from the contralateral position of the same animal (Fig 1B). We also selected another lobster that had substantial ESD showing and which was close to molting to bring into the lab, recorded the day of molt allowing us to sample the animal at a specific time post-molt, Ha7.

Results and Discussion

Chemical analyses

Chemical properties of lobster carapace cuticle architecture were obtained by applying two examplar chemical analytic tools to polished cuticle surfaces. First, using high resolution electron micro-probe, the carbonate apatite exocuticle trabeculae in the lobster carapace exocuticle is demonstrated by its pattern of elemental proportional composition in polished tangential sections of an exocuticle layer. The phosphate, Fig. 2A, is seen in a trabeculum-like pattern on a more uniform pattern of Ca^{2+}, Fig. 2B. Some phosphate rich areas of Fig. 2A have apparent dense cortices with medullas with lowered phosphate density. From geometrically identical sectors of Fig. 2B, the calcium signal, one can recognize corresponding medullas with lowered calcium densities (marked with a white dot). This suggests organized trabeculae develop with cortices of high Ca and P but lower Ca and P at their medulla, a developmental phenomenon that may conserve P and could be confirmed with high-throughput sampling and analysis based on measuring density variation with the more rapid μCT

approach. This analysis was extended to examine other fine resolution tangentially cut structures such as the dermal gland canals, seen in Fig. 3, where an organule canal wall is seen to use two distinct ratios of Ca:P, 2.67 and 2 from Fig. 3E,F, in discrete layers and a third distinct ratio, 3.5, in a secondary-canal wall from Fig. 3C,D.

The patterns of elements used in constructing the carapace can be teased apart using k-means clustering of pixel-wise composition matrices producing a map of clustered pixel types and displayed in raster or bar-chart format, as in Fig. 4. K-means clustering uses a Monte Carlo approach which requires several iterations of clustering to establish a consistent result. However its output provides additional insights into the carapace structure, e.g. chloride distribution in the endocuticle is seen to oscillate significantly in synchrony with the Bouligand layers of cuticle, Fig. 4C, while the calcium, phosphate and Ca:P ratios are not significantly different, Fig. 4B,D,E. It is likely that the chloride content is a basis for endocuticle Bouligand layers being clustered differently, which is repeated in all iterations (not shown) of the k-means clustering algorithm. Three observed k-means clusters regularly spanned the phosphate rich trabeculae seen as the three bars labeled C*anal*, N*ipp* and L*am_2* because they respectively here, in Fig. 4, characterize (1) the majority of the length of the dermal gland canal wall and the cortex of the trabeculae (yellow). (2) the next most phosphate rich structure, the nipple structures (violet), which characterize and surround the exit of the dermal gland canals on the basal side of the cuticle. (3) the lowest phosphate rich structures (brown) which here in Fig. 4A form a continuum with the endocuticle clusters and share with them an enrichment with chloride. The k-means clusters create cartoons of the trabecular cortices and medullas referred to in the previous paragraph. The yellow cortex around a lavender medulla surrounding the dark-brown inner medulla form cartoons replicated through the exocuticle of Fig. 4A, characterizing the trabecular structures. The light brown stalactite material extends from the calcite layer toward the endocuticle and typically merges with dark

224 brown material of the endocuticle layers. Both light and dark brown cluster pixels are lower in
225 chloride.

226 Given that this k-means cluster analysis only covers the three elements Ca, P and Cl, it is possible
227 that distinctive properties of shell structures are established by other elements or chitin and layer-
228 specific protein polymers that participate in the structures. It is known, for instance, that fluoride
229 modifies the luminal surface of dermal gland canals of both *H. americanus* and *Homarus gammarus*
230 (Kunkel et al. 2013), perhaps participating in a similar hardening of carbonate apatite as generally
231 recognized for vertebrate teeth and bones. In addition Mg participates in the calcite layer more so than
232 in the $CaCO_3$ rich structures of the exocuticle, endocuticle and membranous layer (Kunkel et al. 2012).

233 A major insight into the chemical differences between carapace cuticle structures can be obtained
234 from a second analytical method, micro-Raman spectroscopy. The wavelength of the laser photon
235 stimulus is re-emitted as characteristic Raman-shift photons which characterize the molecular bond
236 vibration emitting the photon. The bonding-signature Raman-shifts of carbonate, phosphate and
237 organic structures were evaluated in polished sections of carapace cuticle at an approximate 2 μm
238 resolution using the Labram Aramis micro-Raman spectrometer with auto-focus and auto-cosmic-ray-
239 filter. Fig. 5 illustrates average spectra whose constituent spectra were identified from the raster of
240 collected spectra and were identified using svd analysis. The canal wall of a dermal gland, Fig. 5A,
241 was identified using svd, Fig. 5B, and a mask created, Fig. 5C, picking the spectra to average. The
242 canal wall spectral averages, Fig. 5D-c, showed spectral signals at ν1, ν2, ν4 of PO_4^{3-} and ν1, ν2, of
243 CO_3^{2-} consistent with carbonate apatite, Supplementary Table S1.

244 Similarly the canal lumen exhibited spectra with a dominant peak at wavenumber 1318 cm^{-1}
245 which when averaged, Fig. 5D-a, suggests the canal luminal secretion contains the CH bonding of

246 protein chains. The rings surrounding the canal wall represent alternating phosphate rich and $CaCO_3$
247 rich bands which when averaged provide respectively the trabecular-like spectra, Fig. 5D-e, and $CaCO_3$
248 spectra, Fig. 5D-d. Reference bone and aragonite samples are provided to provide positive controls of
249 standard Raman spectral shifts.

250 Signatures of chitin and protein polymer residues are more clearly seen in supplementary Fig. S3
251 which has its wavelength axis extended to 3500 cm^{-1} and includes the broader ch-stretch regions
252 surrounding 2883 (chitin), 2935 (CHO polymers), and 2965 (protein side-chains). In addition Fig S3
253 demonstrates the Raman spectra of the carapace calcite layer showing its lack of any substantial chitin
254 spectral signal, which characterizes it as a cuticular pre-chitin-synthesis product, marking it as part of
255 the epicuticle.

256 Other analytical techniques can be applied to 2-D polished surfaces of cuticle sections such as
257 micro-FTIR to examine bonding (Kunkel unpublished), polarized light microscopy to examine the
258 calcite layer thickness and orientation (Kunkel et al. 2012) and atomic force microscopy to examine
259 layer structure textures (Kunkel 2013). These techniques are useful in further understanding the
260 properties of cuticle layers but are similar to all other 2-D surface approaches in being too time
261 consuming in preparation and measurement to allow high throughput data collection. These 2-D
262 chemical-analytic approaches however allow us to pursue identified and characterized structures using
263 the more rapid X-ray scanning of cuticle voxel density available via μCT.

264 Exploring Shell 3-D Density using μCT

265 Lobster shell medallion samples for μCT analysis can be produced, scanned and the resultant data
266 analyzed to produce 3-D voxel density data files in a high-throughput mode (18 samples per day) using
267 plunge-freeze fixation and an automatic sample loader of the Skyscan 1272 μCT. The interpretation of
268 the gigabytes of data from each sample could limit the speed with which structures within the voxel

density data can be identified and analyzed. We used an initial exploratory mode to identify software and analytic approaches that could be useful in understanding the structures involved as well as approaching high-throughput speeds for studying natural populations of lobsters.

The surface of the carapace seen on a one week post-molt medallion shows regularly spaced organules. Supplementary Figure S4 shows the entire early postmolt Ha7 medallion scanned at 2.5 μm with μCT. Freeze fixation was able to fix an apparently active stream of secretion coming from openings of the dermal glands of primary and tertiary organules. These freeze-fixed streams of material likely correspond to additions to the 'cement' layer described by Wigglesworth (1948) and Locke (1961) as post-molt dermal gland additions to the epicuticle. We suggest that a secretion, dense enough to be profiled by the X-ray beam, is fixed in the process of being distributed onto the epicuticle surrounding each dermal gland. Fig. 6A illustrates a region-of-interest of the supplementary Fig. S4 medallion processed with the ImageJ Volume Viewer plugin showing a tertiary organule with 4 streams of material emanating from dermal gland canals. In Fig. 6B the voxels are analyzed by the 'Thickness' routine of the BoneJ plugin of ImageJ, which fits spheres of largest possible radius into voxel volumes defined using a 3-D binary segmentation of the X-ray densities. The diameter of a circle fit into a 3D segmented space is presented as a graded-color, small-(dark/purple) to large-(light/yellow). This automated segmentation technique, filling the segmented spaces with graded circles, is relatively time consuming in machine time when applied to an entire stack of voxel slices but provides insight into the uniformity of structures and their thicknesses and could be applied to a small selection of slices to save time. The Fig. 6 demonstration of a thickness measure was carried out in ImageJ including preprocessing by an initial density segmentation to a binary interpretation of the greyscale density after various levels of smoothing of the voxel data to fill interfering natural-low-densities in otherwise regular structures. This pre-processing adds a time consuming step of required

292 investigator attention. The thickness of the elements of the circle-filled 3-D binary structures can be
293 characterized by statistics on the circle diameters or visually as in Fig. 6B.

294 The binary segmentation and thickness analysis protocol, applied to the seven day post molt data,
295 suggests that the calcite layer of the post molt carapace is initially relatively uniform in thickness
296 throughout the viewed surface despite it being from a prior ESD individual. The same thickness-
297 evaluation protocol was applied to three medallions illustrated in Fig. 7. One sample was from C4
298 lobster medallion Ha2 (Kunkel et al. 2016) that did not display any lesions anywhere on its carapace,
299 Fig. 7A. A second medallion Ha7, Fig. 7B, was from a lobster seven days after a molt that had
300 displayed substantial carapace lesions in the prior instar. A third medallion Ha5, Fig. 7C, did not
301 display lesions on its 6 mm diameter surface, but was from a C4 lobster that was displaying ESD
302 carapace lesions elsewhere on the carapace. It is clear that the Ha5 Fig. 7C medallion, from an active
303 ESD lobster, had thinned calcite regions in its apparently non-lesioned areas of the carapace. The
304 apparently-healthy Ha2 lobster cuticle, Fig. 7A, shows relatively uniform thickness calcite layer and
305 the recently molted medallion sample Ha7 Fig. 7B, molted from a formerly ESD lobster, also showed a
306 uniform thickness calcite layer. The serious degree of thinning seen in the Ha5, Fig. 7C, medallion is
307 emphasized by the supplementary Fig. S4 link to a movie displaying an entire stack of the thickness
308 interpretation of the middle zone of the complete hemi-medallion at 2.5 μm resolution showing 1450
309 slices of the thinning phenomenon. While convincing, such comprehensive coverage is time
310 consuming to calculate (at least one day of preprocessing to create a binary segmentation of the calcite
311 layer for each entire medallion sample) and evaluate. A potentially automatic ImageJ protocol for
312 preprocessing random voxel sections could logically be developed to speed this approach to a level
313 which might allow high throughput.

314 Both the Volume Viewer plugin and Bone Thickness plugin of ImageJ provide their insight at a

substantial time cost, partly due to many of the decisions needing to be made by a human operator and partly due to the immense number of calculations that need to be done if the operator chooses comprehensive analysis of all the data, which would be statistically over-scrupulous and impossible to use as a high-throughput protocol. Similarly, a commercial medical software, AnalyzePro was used to segment the data into density defined surfaces that provide useful insights into the carapace architecture by creating stl files, which were used to display the surfaces selectively as digital images. For example, Fig. 8 illustrates AnalyzePro produced stl files of the calcite layer and of the trabeculae of two late intermolt, stage C4, carapace medallions of an ESD lobster, the Ha5 medallion, Fig 8A, B, only superficially lesion free and shown in supplementary Fig. S5 which links to a video, where a hint of a subclinical lesion is suspected as a segmented white patch visible during rotation. The Ha4 medallion, Fig. 8C, D, exhibits the smallest superficially visible lesion we have studied in detail so far. The stl surface plots were embellished with outlines of its dermal gland canal structures obtained with the ImageJ line tracing function which allows tracing of an object through a stack of slices. One feature of Fig. 8C, D medallion ROI and the videos of the rotating structures, provided in supplementary Fig. S6, is the thinned calcite layer, as segmented in ImageJ at a chosen density of calcite, and seen to be very thin in several areas. One can see through fenestrations of the calcite-segmentation to what would be a next layer down, the exocuticle stalactite densities, which we did not visualize in Fig. 8C, D. However, we do see the visualized trabeculae further below in the supplementary Fig. S6, particularly when in motion in the Fig. S6 linked video. Again, this segmentation approach producing stl files is expensive as a commercial software and in analysis time, taking on the order of two computation days for each medallion examined with Analyzer Pro on a fast computer (2.5 GHz, 8 cores) with large memory (16 Gb). It also requires substantial interpretation time to view the motion videos and visually interpret the thinned fenestrated surface. While some economy of effort and time might be achieved when the segmentation of interest is reduced to routine, it is unlikely that this approach would provide successful

high-throughput discrimination between healthy *vs*. ESD prone cuticle. It does however direct one, in this case, to focus on developing a protocol to measure the thickness and density of the calcite layer in a random way to capture the generally pervasive calcite-layer-thinness that may be associated with vulnerability to ESD.

A rapid measure of calcite layer properties was applied, using a standard protocol of ImageJ. Specimen density can be measured along a linear transect averaged with a chosen scan path pixel-width. This approach uses the ImageJ decision path, *Analyze*/*Plot Profile*, to record a linear path oriented perpendicular to the cuticle surface through all the layers and routinely including a reference crystal material, Fig. 9. This approach is relatively easy to implement on medallion voxel sections. It can be automated using a Java Macro defined as an ImageJ plugin. Such an approach would produce data transects (stored as csv files) of voxel density in a linear path through the cuticle, which could be viewed individually, e.g. Fig. 9 A, B and C, or used to provide statistics on the average calcite layer thickness or density distribution, Fig. 9 D, for each medallion. The ROIs need to be identified manually by an operator in the chosen scans, Fig 9A,B, scanned with the ImageJ Analyze/Plot Profile function and the saved profile integrated with an R script function. Figure 9 data includes 318 ROI density averages covering standards, unknowns and baseline. The resultant relative data was analyzed by Analysis of Dispersion and the Multivariate Test of Additional Information (Rao, 1965) implemented in R. The log densities of the scanned included mineral standards (apatite, calcite, KH2PO4, and K phthalate) were used to create a standard curve from the parallel 8- and 16-bit data which was used to estimate the apparent densities of the epicuticle calcite layer and endocuticle measure densities. The barchart of Fig 9D averages over the operational variables bit-depth and scan-width to provide estimated mineral densities for epicuticle and endocuticle for the 4 ESD medallions and three μCT densities (1, 2.5 and 5 μm). It shows, with 95% CI of the means, a largest estimate for

362 epicuticle density when using the highest resolution voxels (1 μm) and a significant trend down with
363 voxel size. This is logical since the epicuticle is a thin layer to begin with and the width of the scan
364 process can blur the peak of density of the thin layer. The endocuticle shows less of that inverse
365 relationship which is also logical given it is a thick layer and the resolution should not matter. This is
366 confirmed by a test of interaction between resolution and cuticle layer which is very highly significant
367 ($P < 0.001$). The covariates of data bit size (8 vs 16) and linear scan path widths (4, 8, 16, 32, 64, 128
368 and 256) chosen in ImageJ did not add any additional information ($P > 0.5$) in estimating the averages
369 of either epicuticle or endocuticle. In a separate series of scans (not shown) scan path width did
370 provide a more stable mean based simply on increasing the number of voxels averaged but did not
371 significantly change the average densities measured. That means one can use the largest scan width
372 that provides the best coverage of a voxel slice and shell layering without including surface features
373 such as pits and gland canals. Using this approach on random μCT voxel sections of each of 18
374 medallions one could process all the medallion data scanned overnight potentially during the following
375 day.

376 In this case, Fig 9, of limited samples the overall densities of the 4 medallion epicuticle-calcite-
377 layers were only modestly different, which is reasonable given that medallions Ha4, Ha5 and Ha6 were
378 from the same C4 stage lobster. The Ha7 medallion was from a recently molted lobster but its calcite
379 layer and endocuticle still showed characteristic densities similar to the Ha4, Ha5 and Ha6 medallions.
380 There was significant interaction between specimen, layer and density which emerges in the barchart
381 Fig 9D as a visible carapace-versus-chela endocuticle density difference. The chela endocuticle is
382 substantially denser as well as being measurably thicker which mark the chela as a potential site of both
383 calcium and carbonate storage, some resorbed before molting the remainder eaten soon after molting.

384 The appearance of lobster populations with carapaces exhibiting some measure of thinned calcite

layer or reduced storage density of minerals in any of the shell layers of exo- or endo-cuticle could be predictive of vulnerability of that population to shell disease. This predictive approach would depend on validating the prediction using populations that are systematically followed and carapace medallions sampled, subjected to μCT and properties of the cuticle correlated with the ensuing history of that population with respect to ESD. The current phase of the study demonstrated an ability to collect quantitative density data that can be analyzed using factorial design and allows significance testing to measure effects of environmental factors on cuticle properties.

Recognizing incipient ESD lesions

To identify a causative agent of ESD we would need to extrapolate to an earliest lesion and identify its association with some causal factor. We have attempted to do that and were frustrated in how time-consuming the extrapolation would be when applied to candidate populations. Here are observations that led to that conclusion

We constructed an ImageJ Volume Viewer interpretation of μCT data from an individual stage C4 lobster Fig. 1B carapace medallion Ha4, displayed in Fig. 10A, which included an approximate 500 μm ESD lesion. Medallion Ha5 was extracted from a symmetrical position across the midline and was superficially free of lesions. Both medallions were examined for calcite layer density and thickness. In addition medallion Ha6 was sampled from the large chela of the same animal, which also had a small ESD lesion. The density reconstructions of the surfaces are illustrated in Fig. 10.

Fig. 10A illustrates the smallest clearly recognizable ESD lesion we have visualized with μCT so far. It is typical of carapace ESD lesions in showing a cylindrical penetration through the epicuticle and exocuticle. The same ImageJ visualization protocol was applied to a larger lesion on the chela medallion, Fig. 10B. The conical chela-lesion has a diameter at the chela cuticle base surface of 250 μm and widens to 1500 μm at the cuticle surface. This chela lesion illustrated, Fig. 10B, is dominated

by the conical endocuticle erosion at a late stage in the ESD development process. Further effort was made to search for lesions in the cuticle sampled from the carapace of this shell diseased lobster that had surrounding cuticle with advanced ESD lesions. One, somewhat questionable, much smaller potential lesion is seen as a departure from regular texture interpreted by Volume Viewer in supplementary Fig. S5. That lesion is of possible further interest in that it potentially shows a decrease in mineral density ballooning internal to the outer surface that could signal some type of penetration through a narrow imperfection in an otherwise relatively tight calcite layer surface. Searching for such irregularities as candidates for the origin of an ESD lesion is fraught with many subjective decisions based on subtle visual interpretations and we did not see this approach as plausible to follow in a quantitative way.

Conclusions

A major message of this study is that μCT can be tremendously informative in exploring the imperfections in structure and development of the lobster cuticle. In particular, high throughput μCT of carapace-cuticle-medallions of the American lobster is suggested as an approach of choice to study lobster ESD-susceptible cuticle. Chela-cuticle-medallions are a poor object from which to obtain high resolution structural data on the relatively thin calcite and exocuticle layers due to the massive endocuticle thickness and dominance of the endocuticle in the total chela cuticle structure. Indeed the calcite and exocuticle layers of the chela are similar in thicknes to those in the carapace. However the massive endocuticle of the chela creates shadow-blurring of the information in the relatively thin epicuticle- and exocuticle-computed voxel densities. The shadow-blurring of surface data would thus decrease the effectiveness of using chela medallions in searching-for and detailed-characterizing of early subclinical lesions. However, measuring chela mineralization may be a valuable indicator of stored $CaCO_3$ that is passed on to the next stage.

Thinness of the calcite layer viewed in the carapace may be a diagnostic feature of vulnerability to ESD. In our admittedly limited study, calcite layer thinness is seen to be correlated with ESD and could also be diagnostic in a predictive sense of individuals that do not yet display ESD at all or in other regions of their cuticle. To establish this prediction-objective one would need to apply this approach in a truly high-through-put manner in populations that predictably would develop high ESD incidence, but now in analysis are lobsters that are superficially ESD free.

Seeing and characterizing a sub-clinical ESD lesion itself may not be a realistically achievable and quantifiable objective to use in predicting population-vulnerability to ESD. It would require scanning too large an area of carapace cuticle at high resolution. The protocols to analyze the data to see the smallest lesions would be too time consuming in our experience. This might change with faster more powerful computers. Rather, characterizing the calcite layer thinness or density is an achievable diagnostic feature that may define lobster cuticle health and the ability to predict the vulnerable fraction of the lobster population that will develop shell disease.

We show that a healthy calcite layer has the approximate density of KH_2PO_4, used as a calibration standard. This implies that there is additional lower density material in what we describe compositionally (Kunkel 2106) as a calcite layer, lowering its density from 2.71 g/cm^3 to 2.34 g/cm^3 of KH_2PO_4. This approximate density was seen in all the so-called healthy cuticles observed in this study including calcite layers adjacent to ESD lesions. This emphasizes the fact that the cuticle adjacent to ESD lesions seems to maintain a reasonably characteristic and healthy density despite being in an ESD animal and even close to the edge of an ESD lesion. This also puts more emphasis on the thinness of the calcite layer rather than its density. Clearly these characterizations need to be tested more comprehensively by studying a variety of carapace medallions from more populations of characterized health. With larger sample sizes including the density standard may be an important reference to add

accuracy to density measurements. The density feature, evaluated in high throughput samples using μCT, in itself may turn out to be one standard of cuticle wellness that can be used diagnostically to evaluate a population's future vulnerability to ESD. In addition, the K bipthalate density standard used (1.64 g/cm^3) was found to be very close to the endocuticle density making it an important reference for measuring endocuticle density variation.

Using Raman spectrometry, which did not detect chitin in the calcite layer of the carapace cuticle, the calcite layer is now clearly shown to be a part of the lobster carapace epicuticle. That layer clearly develops its mineralization after ecdysis, including the post-ecdysial application of cement from the dermal glands. This agrees with the concept of the arthropod cuticle being a living compartment of the organism that develops in many ways post-ecdysis (Wigglesworth 1948, Locke 1961). The living-cuticle concept opens further questions about functions of macromolecules associated with lobster epicuticle/calcite layer formation (Kunkel, 2013). Of particular interest would be characterizing the macromolecules, organic materials and potential mineral components added as the cement layer to the epicuticle from the dermal glands, which are seen to be X-ray dense enough to be clustered as a cuticular component in canal contents (Kunkel et al. 2016 Fig. 6A) as well as here, Fig. 5D-a and Fig. 6A,B.

Irrespective of cuticle microbial flora (Feinmann et al, 2017), it is likely that vulnerability of the cuticle to widely distributed flora will control whether ESD actually develops. If environmental stressors such as ocean acidification creates a population of lobsters with increased vulnerability (e.g. due to thinness of the calcite layer) it is more likely that an opportunistic bacterium can nucleate the original subclinical lesion needed to allow ESD to develop.

The nature and causes of shell vulnerability need to be studied further. The newest model of the lobster carapace cuticle provided here, Fig. 11, includes our latest insights into lobster shell that is the

target of ESD. The features of this model were developed from observations on the cuticle made by many past investigators (reviewed by Kunkel, 2013) with newer insights reported recently (Kunkel et al. 2016) as well as here. Many features of the model could contribute to vulnerability and development of shell disease. The immediate cause of shell disease may be the local thinness of the calcite layer which allows a specific microbe, a combined consortium or dysbiosis of microbes (Meres et al. 2012) to attack, causing a subclinical lesion that is widened into a recognizable lesion by an even greater variety of microorganisms (Bell et al. 2012).

However the underlying cause of ESD may derive from various sources. One cause could be the lack of sufficient $CaCO_3$ and carbonate apatite precursors that needed to be accumulated as cuticle components in the prior instar that would allow, on resorption and reuse, a healthy new cuticle to be established in a timely fashion and promoting an ESD resistant cuticle. Unlike other marine organisms which are dependent on the immediate ocean environment's $CaCO_3$ availability (Zeebe 2012), the lobster creates its shell from internal stores of $CaCO_3$ which depend on how prior stages have faired in accumulation of this valuable marine resource which is being made more expensive to obtain due to ocean acidification. The lobster is one organism that can survive in undersaturated seawater (Lebrato et al. 2016) but our thesis is that the undersaturation may cause a decreased history of storage of $CaCO_3$ in the endocuticle, which is likely a major source of mineral that is resorbed in D1-D3 and stored for biomineralizing the next stage's cuticle. Insufficient $CaCO_3$ or $MgCO_3$ recovery between stages from exo- and endo-cuticle could lead to vulnerability at some point when the recovered minerals from the old cuticle are insufficient to produce a secure new exo-cuticle, which we see as the major structurally rigid protective structure of the cuticle. We also see the endocuticle as a storage depot to allow accumulation of chitin and minerals that are additional mineral and polymer resources needed to allow for the, in general, 10 percent linear growth and 20% area growth of new exo-cuticle that happens

500 suddenly at ecdysis in each molting cycle. This deposition and resorption of $CaCO_3$ is seen as an
501 energetic process that crustaceans must undergo every molting cycle (Ziegler et al. 2012, 2017). But in
502 each molting cycle they must reinvest extra chitin and minerals rapidly after ecdysis in a new
503 exocuticle from an adequate resorbed resource that includes extra $CaCO_3$ derived by resorption from
504 the prior cuticle including endocuticle and membranous layer $CaCO_3$ deposits. In addition the lobster
505 eats its own shed cuticle soon after ecdysis which has residual $CaCO_3$ and $MgCO_3$ already in its proper
506 carbonate oxidation state. This adds to a lobsters natural diet which includes shellfish high in mineral
507 carbonates. Previous use of μCT (Kunkel et al. 2016) has identified structures such as the stalactites in
508 the exocuticle, Bouligand spirals in the endocuticle and basal granules in the membranous layer which
509 appear, based on their density, to be composed of $CaCO_3$ that exist during the C4 stage of intermolt
510 and which would likely be sources of resorbed $CaCO_3$ as molting is initiated. EMP scans of these
511 layers at stage C4 (Kunkel, 2012) also demonstrate a substantial molar ratio of $MgCO_3$ that is
512 contained in the inner layers of cuticle available for polymer and mineral resorption and reuse.
513 Interestingly, the C4 lobster providing Ha4, 5 and 6 medallions, from the high ESD area was not seen
514 to have the membranous layer $CaCO_3$ basal granules and Bouligand spiral extensions of exocuticle
515 stalactites into the endocuticle that were seen in the ESD population lobsters from outer Georges Bank
516 (Kunkel 2016). If the environmental availability of those minerals does not allow the endocuticle and
517 membranous layers to accumulate the extra stored minerals, then the needed resources to establish an
518 invulnerable new exocuticle may be lacking in a vulnerable population of lobsters. This stored-
519 mineral-aspect of vulnerability may build up over a series of molting cycles until it becomes critical
520 and the cuticle's vulnerability is breached by perhaps the normal cuticle flora or by encouraging a
521 dysbiosis (Meres et al. 2012).

522 Another avenue to shell vulnerability could be an improper application of the cement layer that

was visualized here being applied onto the new cuticle from dermal glands. The composition of this post-ecdysial applied component of the epicuticle has been shown to be of sufficient density to be detected with the X-ray dose that images the main mineral cuticle. In fact the density of the canal contents is similar to that of the lobster's endocuticle (Kunkel et al. 2016). The cement is also independent of the contribution that is traditionally considered to be applied to the epicuticle from the pore canals which service the epicuticle from the inside (Locke, 1961).

The observation that a seemingly healthy-thick calcite layer was seen in a new cuticle, medallion Ha7, sampled from a prior stage ESD lobster, Fig. 7B, argues that environmental erosion of the calcite after this early phase of the new cuticle may be important to ESD vulnerability. It could be also due to a clinically improper application of the post-molt protective cement layer. Measuring the post-ecdysial thinning of the calcite layer, due to ocean acidification, is one potential avenue of research that may provide insight into the development of vulnerability. Using a high throughput procedure like μCT to follow carapace cuticle development and correlating it with local contemporaneous historical environmental data, such as temperature, calcium availability and pH in that lobster's experience, may be the only way we can understand how and why ESD develops in one local population and not in another.

The ESD prediction approach depends on both a high-throughput data sampling method, such as the particular model of μCT used here that provides a multi-position autosampler, but also depends on rapid high-throughput-analysis. We examined several analytic protocols, which were informative on individual specimens, but which were too time-consuming to be dynamically applied to keep up with a high sampling rate. We compared the slow-methods to methods that are directed at rapidly establishing statistics such as thinness or density of the calcite or other layers. Collection of μCT data from lobster carapace medallions sampled from lobsters of different developmental stages from different

546 populations of variable ESD vulnerability would create a database as described in previous structural
547 studies (Shields et al. 2012, Kunkel et al. 2016). Earlier contributions of cuticle structural detail to such
548 a database resource was not feasible due to the preparation and analysis time but μCT of plunge frozen
549 cuticle medallions may provide the high enough throughput that enables structural data to be
550 accumulated for such a database. It would allow tailor made rapid questions to be asked using fast
551 ImageJ macros that could mine the data to test hypotheses on determinants of ESD, some of which
552 have been presented here. We argue here for the enhancement of such a database with μCT data with
553 appropriate metadata on age and environmental parameters that can help understand current lobster
554 population vulnerabilities as they change.

555 Acknowledgements

556 The research associated with this project was supported by NOAA grant NA06NMF4720100 to RI
557 SeaGrant supporting the New England Lobster Research Initiative. Vertebrate bone reference material
558 was dissected and provided by P Pajevic.

559 Literature Cited

560 1. Bell SL, Allam B, McElroy A, Dove A, Taylor GT. (2012). Investigation of epizootic shell
561 disease in American lobsters (*Homarus americanus*) from Long Island Sound: I.
562 Characterization of associated microbial communities. Journal of Shellfish Research 31(2), 473-
563 484. https://doi.org/10.2983/035.031.0207

564 2. Hostens J, Laperre K. (2015). High resolution microCT in preclinical applications.
565 https://www.bruker.com/service/education-training/webinars/pci-webinars/high-resolution-
566 microct-webinar.html (last accessed Oct 20, 2017).

567 3. Castro KM, Factor JR, Angel T, Landers Jr. DF. (2006). The conceptual approach to lobster

shell disease revisited. J Crust Biol 26(4): 646-660. https://doi.org/10.1651/S-2761a.1

4. Castro KM, Cobb JS, Gomez-Chiarri M, Tlusty MF. (2012). Epizootic shell disease in American lobsters *Homarus americanus* in southern New England: Past, present and future. Dis. Aquat. Org., 100(2):149–158. https://doi.org/10.3354/dao02507

5. Feinman SG, Martínez AU, Bowen JL, Tlusty MF. (2017). Fine-scale transition to lower bacterial diversity and altered community composition precedes shell disease in laboratory-reared juvenile American lobster. Dis Aquat Org 124(1): 41–54. https://doi.org/10.3354/dao03111

6. Glenn RP, Pugh TL. (2006). Epizootic shell disease in American lobster (*Homarus americanus*) in Massachusetts coastal waters: Interactions of temperature, maturity, and intermolt duration. J Crustacean Biol 26(4): 639-645. https://doi.org/10.1651/S-2754.1

7. Kozielski M, Buchwald T, Szybowicz M, Błaszczak Z, Piotrowski A, Ciesielczyk B. (2011). Determination of composition and structure of spongy bone tissue in human head of femur by Raman spectral mapping. Journal of Materials Science: Materials in Medicine 22(7): 1653–1661. https://doi.org/10.1007/s10856-011-4353-0

8. Kunkel JG. (2013). Modeling the calcium and phosphate mineralization of American lobster cuticle. Can. J. Fish. Aquat. Sci. 70(11): 1601-1611. https://doi.org/10.1139/cjfas-2013-0034

9. Kunkel JG, Jercinovic MJ, Callaham DA, Smolowitz R, Tlusty MF. (2005). Electron microprobe measurement of mineralization of American lobster, *Homarus americanus*, cuticle: Proof of concept. 2005 Lobster Shell Disease Workshop, UMass Boston, MA. New England Aquarium. Aquatic Forum Series, pages 76-82. (accessed Aug 3, 2017). http://www.bio.umass.edu/biology/kunkel/pub/reprints/LobsterWorkshopMS-jgk.pdf

10. Kunkel JG, Nagel W, Jercinovic MJ. (2012). Mineral fine structure of the American lobster

cuticle. Journal of Shellfish Research 31(2): 515-526. https://doi.org/10.2983/035.031.0211

11. Kunkel JG, Jercinovic MJ. (2013) Carbonate apatite formulation in cuticle structure adds resistance to microbial attack for American lobster. Marine Biology Research 9(1): 27-34. http://dx.doi.org/10.1080/17451000.2012.727427

12. Kunkel JG, Rosa M, Bahadur AN. (2015). Toward a modern interpretation of the American lobster shell using X-ray tomography. The Lobster Newsletter 28(2):19-21. http://www.fish.wa.gov.au/Documents/rock_lobster/the_lobster_newsletter/lobster_newsletter_v28_no2.pdf (last accessed Aug 3, 2017).

13. Kunkel JG, Rosa M, Bahadur AN. (2016). 3D-Xray-tomography of American lobster shell structure: An overview. Fisheries Research 186(1): 372-382. https://doi.org/10.1016/j.fishres.2016.09.028

14. Kunkel JG, Tlusty M, Jercinovic MJ. (2013). Fluoride role in carbonate apatite structures in exoskeletons of clawed lobsters, *Homarus americanus* and *Homarus gammarus*. Aquaculture 2013, Nashville TN. (last accessed Aug 3, 2017) https://www.was.org/meetings/SessionAbstracts.aspx?Code=AQ2013&Session=37

15. Laufer H, Chen M, Johnson M, Demir N, Bobbitt JM. 2012. The effect of alkylphenols on lobster shell hardening. J. Shellfish Res. 31(2):555–562. https://doi.org/10.2983/035.031.0215

16. Lebrato M, Andersson AJ, Ries JB, Aronson RB, Lamare MD, et al. (2016). Benthic marine calcifiers coexist with $CaCO_3$-undersaturated seawater worldwide. Global Biogeochemical Cycles. 30(7): 1038–1053 https://doi.org/10.1002/2015GB005260

17. Locke M. (1961). Pore canals and related structures in insect cuticle. J Biophysical and Biochemical Cytology 10(4): 589-618.

https://www.ncbi.nlm.nih.gov/pmc/articles/PMC2225106/

18. Mandair GS, Morris MD. (2015). Contributions of Raman spectroscopy to the understanding of bone strength. BoneKEy Reports 4(620):1-8. https://doi.org/10.1038/bonekey.2014.115

19. Mandel C. (2016). New England lobsters swim to Canada, bringing jobs with them. National Observer 2016 June 1. https://www.nationalobserver.com/2016/06/01/news/new-england-lobsters-swim-canada-bringing-jobs-them (last observed Oct 22, 2017).

20. Meres NJ, Ajuzie CC, Sikaroodi M, Vemulapalli M, Shields JD, Gillevet PM. (2012). Dysbiosis in epizootic shell disease of the American lobster (*Homarus americanus*). J. Shellfish Res. 31(2):463-472. https://doi.org/10.2983/035.031.0206

21. Movasaghi Z, Rehman S, Rehman IU. (2007). Raman spectroscopy of biological tissues. Applied Spectroscopy Reviews 42(5): 493-541. http://dx.doi.org/10.1080/05704920701551530

22. NOAA. (2009) North Cape oil spill. Damage assessment, remediation and restoration program. https://darrp.noaa.gov/oil-spills/north-cape (last accessed Aug 20, 2017).

23. Perry AL, Low PJ, Ellis JR, Reynolds JD. (2005). Climate change and distribution shifts in marine fishes. Science 308(5730), 1912-1915. http://dx.doi.org/10.1126/science.1111322

24. Rao CR. (1965) Linear Statistical Inference and Its Applications. John Wiley & Sons, New York, 522pp.

25. Shields JD, Wheeler KN, Moss JA. (2012). Histological assessment of the lobster (*Homarus americanus*) in the ‘‘100 Lobsters’’ project. Journal of Shellfish Research 31(2): 439–447. https://doi.org/10.2983/035.031.0204

26. Smolowitz R, Chistoserdov AY, Hsu A. (2005). A description of the pathology of epizootic shell disease in the American lobster, *Homarus americanus*, H. Milne Edwards 1837. J

634 Shellfish Research 24(3):749-756. https://doi.org/10.2983/0730-8000(2005)24[749:ADOTPO]2.0.CO;2

635 27. Steneck RS, Wahle RA. (2013). American lobster dynamics in a brave new ocean. Canadian
636 Journal of Fisheries and Aquatic Sciences 70(11): 1612-1624. https://doi.org/10.1139/cjfas-2013-0094

637 28. Stevens BG. (2009). Effects of epizootic shell disease in American lobster *Homarus*
638 *americanus* determined using a quantitative disease index. Dis Aquat Org 88(1): 25–34.

639 29. Tlusty M, Smolowitz RM, Halvorson HO, DeVito SE. (2007). Host susceptibility hypothesis
640 for shell disease in American lobsters. J Aquatic Animal Health 19(4):215–225.
641 http://dx.doi.org/10.1577/H06-014.1

642 30. University of Maine. (2017). Longer, stronger summers in the Gulf of Maine. ScienceDaily, 5
643 September 2017. <www.sciencedaily.com/releases/2017/09/170905202951.htm>

644 31. Waddy SL, Aiken DE, De Kleijn DPV. (1995). Control of Growth and Reproduction. Chapter
645 10 in JR Factor. Biology of the Lobster, Elsevier, pp 217-266.

646 32. Wigglesworth VB. (1948). The insect cuticle as a living system. Disc Faraday Soc 3: 172-177.
647 http://dx.doi.org/10.1039/DF9480300172

648 33. Zeebe RE. (2012). History of seawater carbonate chemistry, atmospheric CO_2, and ocean
649 acidification. Annu Rev Earth Planetary Sciences 40:141–65.
650 http://dx.doi.org/10.1146/annurev-earth-042711-105521

651 34. Ziegler A, Weihrauch D, Hagedorn M, Towle DW, Bleher R. (2004). Expression and polarity
652 reversal of V-type H^+-ATPase during the mineralization-demineralization cycle in *Porcellio*
653 *scaber* sternal epithelial cells. J Exp Biol 207:1749–1756. http://dx.doi.org/10.1242/jeb.00953

654 35. Ziegler A, Neues F, Janacek J, Beckmann F, Epple M. (2017). Mineral in skeletal elements of
655 the terrestrial crustacean *Porcellio scaber*: SRmCT of function related distribution and changes

during the moult cycle. Arthropod Structure & Development 46(1): 63-76.

https://doi.org/10.1016/j.asd.2016.05.004

Figure Legends

Figure 1. American lobster *Homarus americanus* shell diseased carapaces. A. Montage of 22 light microscopy images of cuticle combined to demonstrate finding peripheral small-lesions (<) surrounding major lesions (L). Based on ImageJ measurement, these marked small-lesions are all above 1.5 mm in diameter. Their size can be judged relative to the original lobster in supplementary Figures S5A and S5B. B. Live lobster carapace with measured CL of 58 mm has large merged lesions (L) around the medial dorsal suture, two smaller lesions marked (<) among many and two 6 mm medallion sampling locations, Ha4 and Ha5, patched on the medial lateral carapace. Medallion Ha4 was chosen to include the smallest of small lesions available, with diameter approximately 0.5 mm. Medallion Ha5 on the adjacent side had no superficially visible lesions when sampled.

Figure 2. Selected area analyses of Ca, P and Cl data for trabeculae separating and surrounding three primary organules seen in a tangental polished section of lobster cuticle through the inner exocuticle. A. Phosphate image with 4 sub-areas identified by rectangular boxes. B. Calcium image similarly divided. Low Ca cores are marked with a white dot. C-G. Sub-areas of panels A and B analysis. C. svd_{Ca} of the organule data enclosed by yellow rectangles in panels A & B. D. A mask created by choosing pixels identified with $svd_{Ca} > 100$. E, F, G: The masks identifying phosphate-rich pixels of three areas of panel A and B produced with $svd_{P} > 25$. H. log Ca vs log P are plot with the same standard of fluoroapatite (red line with Ca/P of 5:3), clam shell (green with Ca/P of 1:0) and $Ca(H_2PO_4)_2$ (blue line with Ca:P = 0.5). The 3 sample areas of trabeculae have their means and 1 (broad bar) and 1.96 (thin bar) standard deviations corresponding to 64% and 95% confidence intervals of the data computed on a log normal basis.

Figure 3. Selected area analyses of Ca and P for a secondary organule seen in a tangental polished section of lobster cuticle through the inner exocuticle. A. Phosphate image. B. Calcium image. C-F.

Selected areas of panels A and B analyzed by singular value decomposition which allow apatite and calcite pixels to be identified. G. A scatter-plot of apatite pixel Ca and P vs each other with a standard of fluoroapatite (red with Ca/P 5:3 =1.67), clam shell (green with Ca/P of 1:0) and Ca(H2PO4)2 (blue with Ca:P slope 0.5). The CAp of the large canal, E & F, displays Ca:P dual ratios of 2 and 2.67 (orange) while the smaller canal in C & D, displays a single ratio of 3.5 (purple). The Ca rich enclosing sheath of the canal seen in B and E is likely an organule socket cell product.

Figure 4. K-means cluster analysis of carapace cuticle EMP, alternate analysis of Kunkel and coworkers (2013, Fig. 3) data. A. One of 25 independent iterations of a 10-mean clustering of EMP compositional data of American lobster C3 carapace polished cuticle section. Six clusters (4 ignored clusters were external densities and coded black) span the cuticle structures which are given colors and names typical of their location. The calcite cluster is red and has the highest Ca:P ratio being highest in Ca and lowest in P. The canal cluster is yellow but shares its cluster with trabeculae. The nipple cluster is violet and also shares its cluster with trabeculae. The stalactite cluster is light brown. The endo1 cluster is green. The endo2 cluster is dark brown. Barcharts comparing the cluster properties are presented as panels B-E. B. Ca/P ratios of the cluster pixels. C. Chloride content of cluster pixels. D. Calcium content of cluster pixels. E. Phosphate content of cluster pixels.

Figure 5. Raman spectra of selected areas of lobster cuticle seen in tangental polished section, neonatal mouse bone, purified crab chitin, calcite crystal and cod otolith aragonite standard. **A**. Light microscope image of canal. **B**. svd 3 contrasting the canal wall with other surrounding structures. **C**. Mask identifying locations of spectra with svd > 200. **D**. a. Lobster dermal gland canal lumen average of 38 spectra. b. Canal wall average of 172 spectra. d. $CaCO_3$ ring average of 84 spectra. Spectra b, d, e, f, h: b. Mouse bone reference (from Kavukcuoglu et al. 2009). e. Cuticle trabeculae. f. Chitin standard. g. Calcite crystal. h. Cod otolith aragonite standard average of 25 spectra. Grey highlighted

zones: i. v1 PO_4, ii. v2 PO_4, iii. v3 PO_4 , iv. v1 CO_3, v. v2 CO_3

Figure 6. ROI of medallion Ha7 with an actively secreting organule with secretion streams captured as X-ray densities. A. Oblique view of the ROI interpreted with ImageJ VolumeViewer plugin. B. Oblique view of the ROI interpreted with the ImageJ Bone Thickness plugin with lighter toned structures are thicker.

Figure 7. μCT of three American lobster carapace medallions with their voxel densities interpreted with the Bone Thickness Plugin of ImageJ. **A.** ROI of C4 lobster Ha4 from an ESD free zone. Caret (^) shows a region of relative thinning of the calcite layer. **B.** ROI of 7-day post molt medallion Ha7 from an a lobster with ESD in prior stage. The bright continuous calcite layer (<) is thick even at the interface with the organule canal (>). **C.** ROI of a no-lesion-medallion Ha5 from the ESD lesioned C4 lobster medallion. Lighter color illustrates thicker layer. The carets (^) show regional thinning (coded darker) of the calcite layer that could indicate vulnerabilities to ESD, which is nowhere seen on this medallion Ha5 with the exception of a ROI suggested to be a possible incipient lesion and investigated in Figs 8A,B and seen in supplementary image and video Fig S6.

Figure 8. Structural surfaces of lobster carapace cuticle defined by stl files extracted from μCT of ESD infected American lobster carapace medallions. **A** and **B** are from 6 mm diameter medallion Ha5 that shows no apparent lesions. **C** and **D** are both a ROI from medallion Ha4 with a 500 μm diameter ESD lesion. **A.** 2.5 μm resolution μCT scan that needed to be divided into two hemi-medallion data sets, which were analyzed in AnalyzePro and re-assembled in Meshlab. Potential areas of vulnerability are indicated (<) based on the localized thinned (pink) stl file expression of the calcite layer. **B.** stl files of the calcite and trabeculae are viewed obliquely using an R-library to read and plot stl defined surfaces. A caret (^) indicates a possible incipient ESD lesion color coded in white. Potential areas of vulnerability are indicated (<) based on the localized thinned (yellow) stl file expression of the calcite

727 layer. These are the same vulnerabilities indicated in the panel-A pink sector. **C.** ROI of the ESD
728 lesion as seen with stl file defined density structures of calcite layer (red), trabeculae (green),
729 membranous layer (grey) with outlines of recognizable canal paths (purple). **D.** Same as **C** viewed
730 from above through an imposed transparency of the calcite layer.

731 Figure 9. Analysis of X-Ray density of cuticle layers obtained by ImageJ line scans. A. Image and
732 scan track of Ha6 voxel slice from a dorsal 'crusher' chela with 128 μm and 256 μm wide line scan-
733 tracks. B. Image and scan track of Ha4 voxel slice from dorsal lateral carapace with two 128 μm wide
734 scan-tracks. C. Running averages of the voxel density along transects the R,G & B lines (illustrated
735 with coordinated colors in panels A and B) showing sectors of averages for epicuticle, endocuticle,
736 standards (apatite, calcite, KH_2PO_4 and zero-baseline density) which were averaged to produce a single
737 datum for analysis of variance. D. A barchart of epicuticle density (blue) and endocuticle density
738 (orange) focusing on the effect of μCT resolution on the measurement of epicuticle and endocuticle
739 layer density. Means +/- 95% CI of the mean are plotted. Sample size is displayed parenthetically
740 above the CI bar. The microCT resolution is listed for each specimen on the X axis.

741 Figure 10. ImageJ Volume Viewer interpretations of the μCT data of two 6 mm diameter medallions
742 from a stage C4 animal with ESD. **A.** Carapace medallion Ha4 with a 500 μm diameter lesion. **B.**
743 Portion of a chela medallion Ha6 with a conical shaped lesion developed through the cuticle. Insets
744 show select orthogonal sections.

745 Figure 11. Interpretive model of American lobster carapace cuticle and response to ESD. This model
746 version includes newly observed dynamic post-molt application of the cement layer by the dermal
747 glands, recently described Bouligand swirls in the endocuticle and basal granules in a membranous
748 layer (Kunkel et al. 2016). The cement layer moderates the dissolution of the shell's $CaCO_3$ allowing
749 for an antimicrobial high pH unstirred layer. Aside from the Calcite ($CaCO_3$) layer of the Epicuticle

and the stiff Phosphatic Trabeculae of the Exocuticle, the remaining bulk of the Bouligand layered cuticle is invested with relatively soft amorphous $CaCO_3$, (ACC) co-located with the chitin lamellae (wavy lines) as compact yellow (stalactites) in the exocuticle, seen as more diffuse yellow (Bouligand spirals) in the endocuticle and ending as basal granules in the membranous layer. Regional thinning of the calcite layer may lead to poor maintenance of the high-pH unstirred layer and greater vulnerability to ESD. A shell reacts to a lesion penetrating through the calcite layer by an increased flux (* red flux arrow) of (red/dissolving) ACC, more soluble than the crystalline-calcite form of $CaCO_3$. The more rapid dissolution of ACC increases the unstirred layer pH, an evolution engineered defense against lesion development. As the model fails, opportunistic bacteria and other micro-organisms aggressively digest the cuticle, the animals hemocoel is compromised and it dies.

761 Table 1. American lobsters used in the current study. Each specimen is a 6 mm medallion of cuticle
762 collected using a coring drill, leaving a 7mm hole in the carapace, and plunge-frozen in -40ºC acetone
763 and processed as described. Both ESD animals used came from outer Casco Bay.

Sample	Lobster	Description	µCT sample
Ha4	C4 lobster with ESD	Right medial lateral carapace 6 mm medallion sample with a small 0.5 mm lesion with surrounding clear cuticle. The 7 mm hole in the carapace was patched as described, Fig 1B.	1, 2.5 and 5 µm
Ha5	Same C4 lobster.	Left medial lateral carapace medallion sample one week later than Ha4 had clear cuticle with no apparent lesion. The 7 mm hole was patched as described, Fig 1B.	1 and 5 µm
Ha6	Same C4 lobster	Right crusher claw face was sampled one week after the Ha5 Sample. The 7 mm hole was patched and the lobster maintained in a life table until it molted two months later.	1 and 2.5 µm
Ha7	An ESD lobster was maintained in a life table until it molted. It was sampled 7 days after molting.	Right medial lateral carapace medallion was sampled from the post-molt completely ESD-free lobster cuticle.	1 and 2.5 µm

764

765 Figure 1

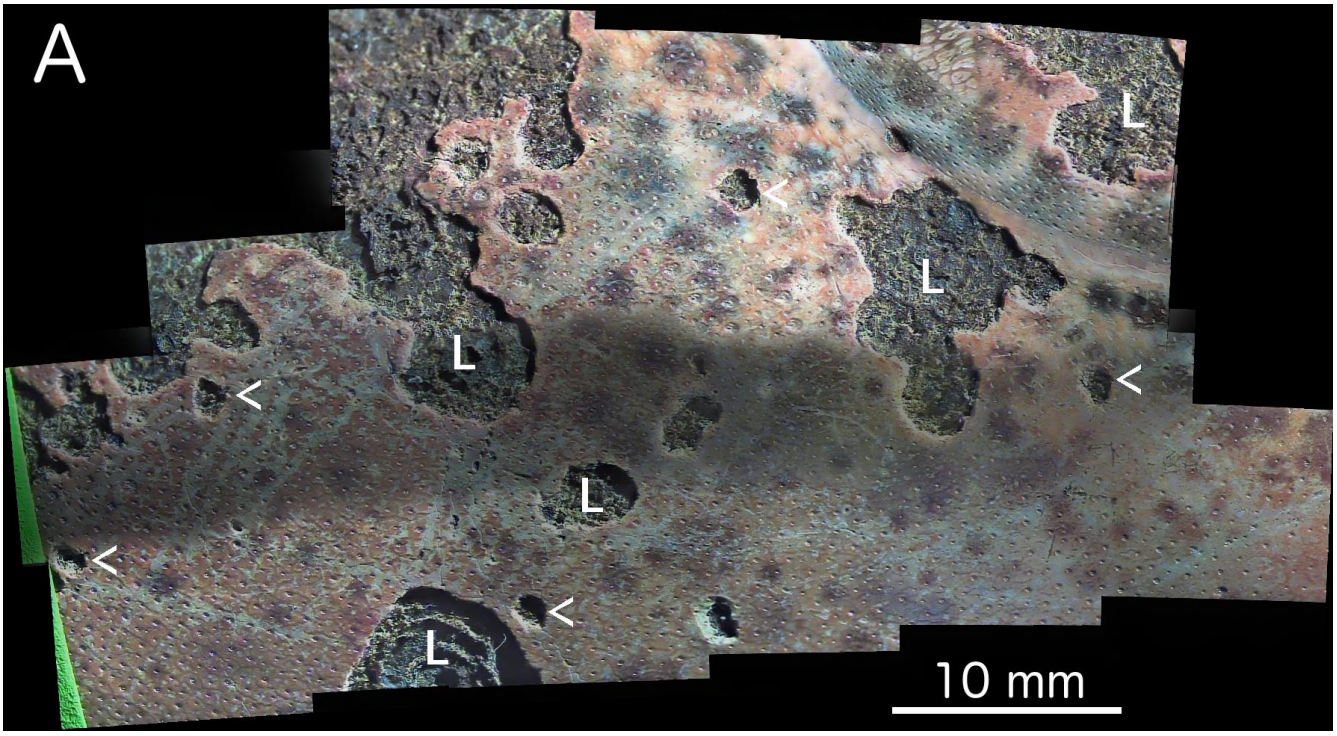

766

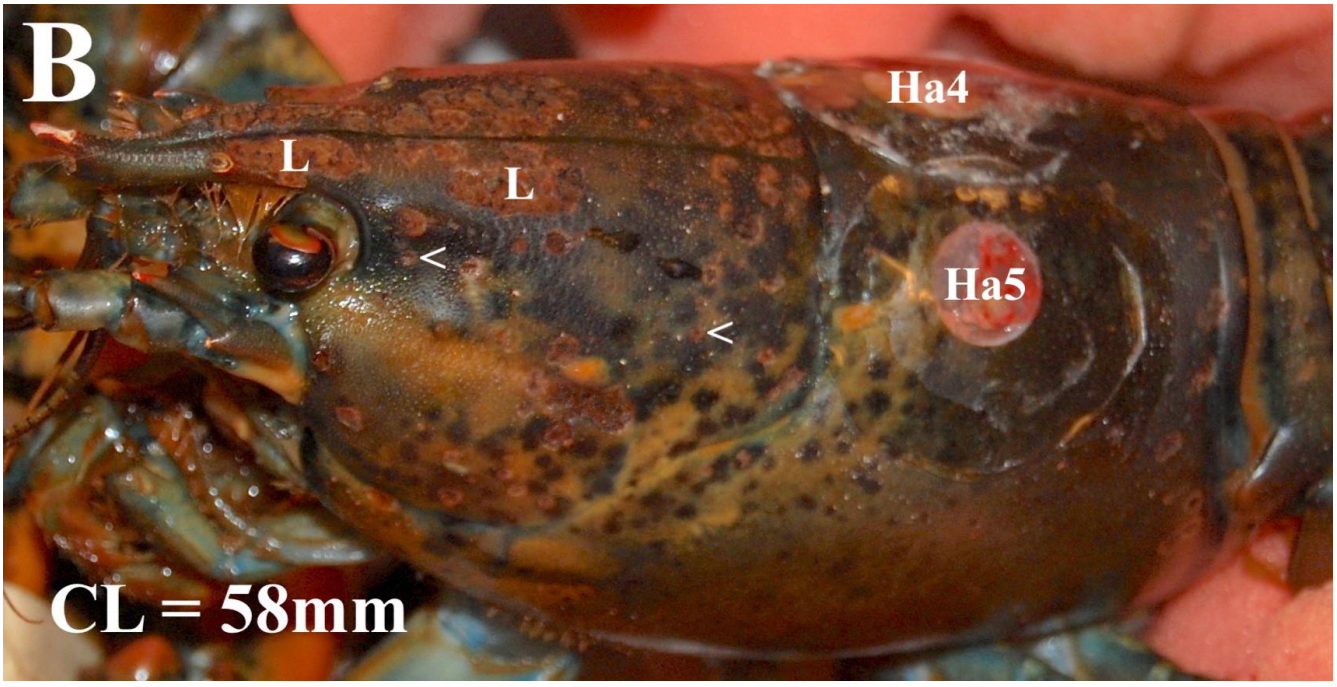

767

768

769 Figure 2.

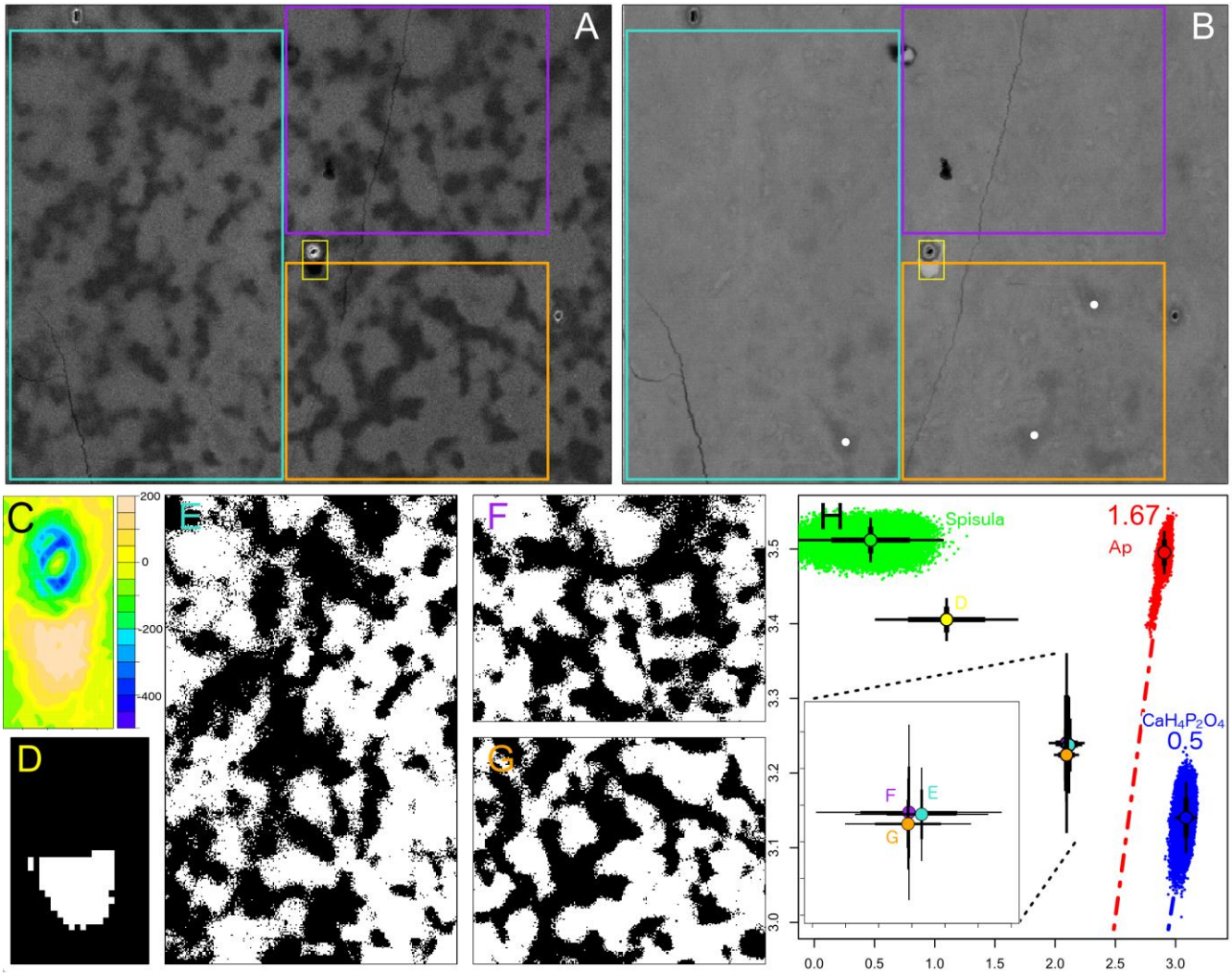

770

771

772

773

774

775

776

777 Figure 3.

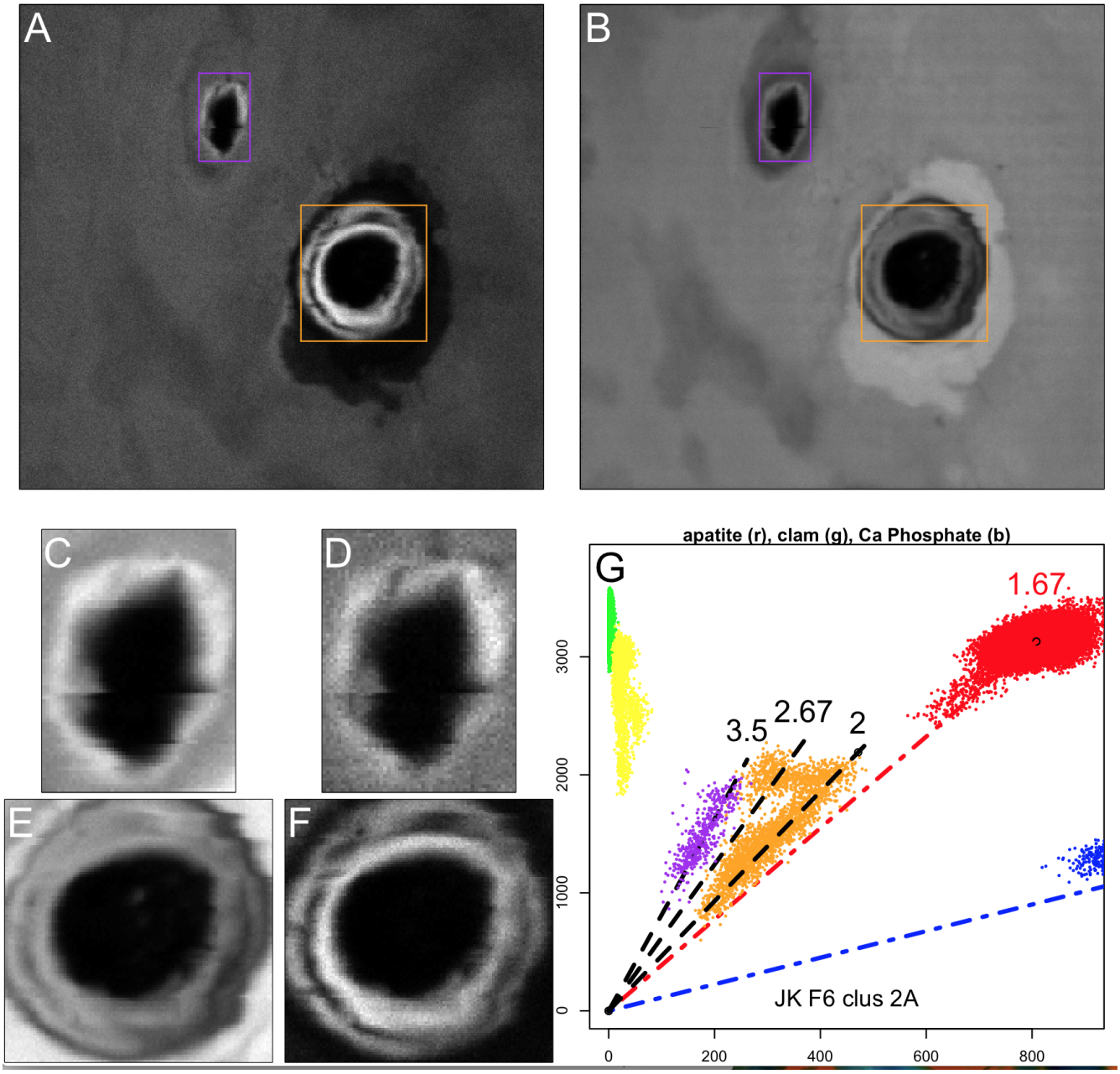

778

779 Figure 4

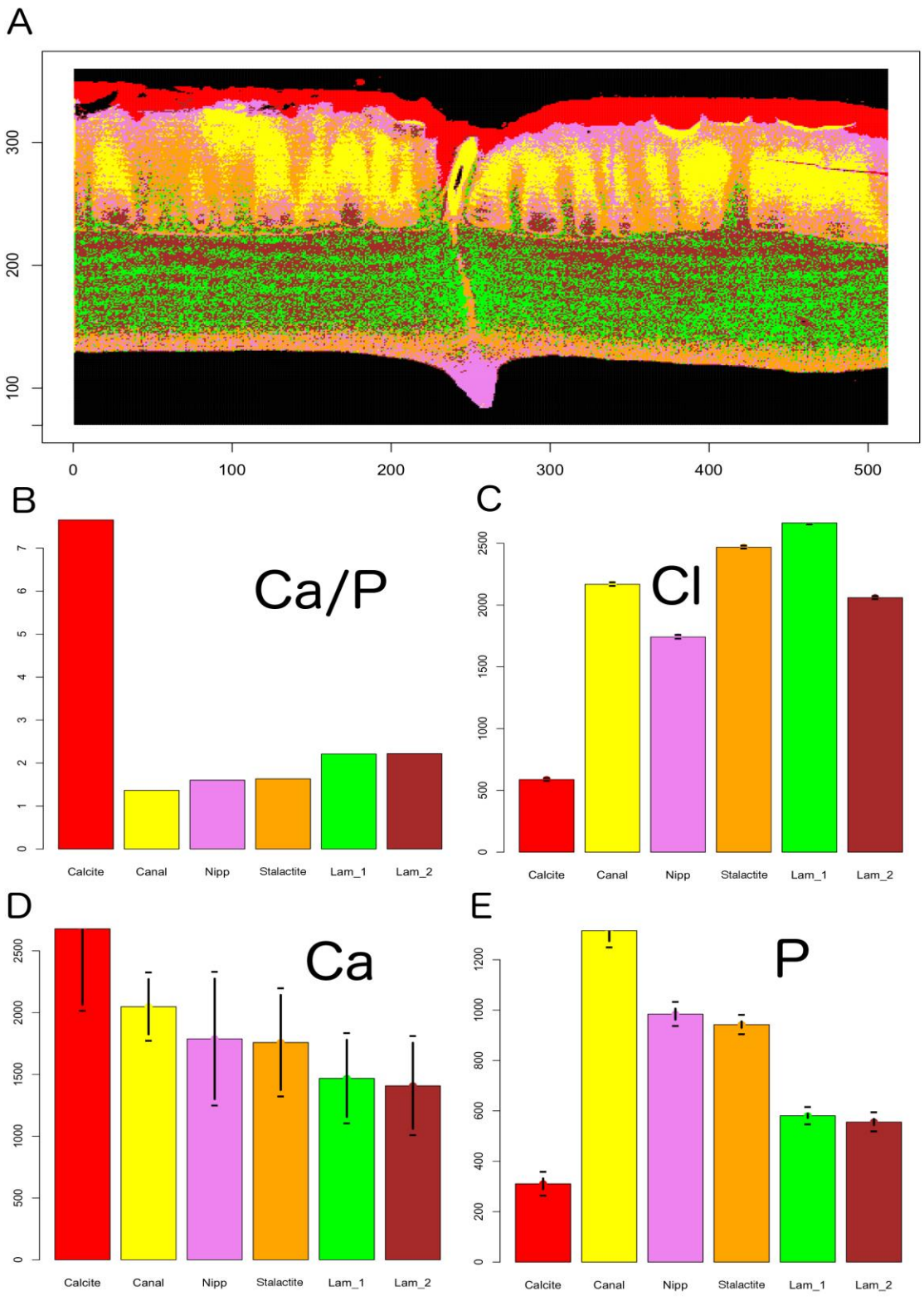
A
300
200
100
0
100
200
300
400
500
B
Ca/P
0
1
2
3
4
5
6
7
Calcite
Canal
Nipp
Stalactite
Lam_1
Lam_2
C
Cl
0
500
1000
1500
2000
2500
Calcite
Canal
Nipp
Stalactite
Lam_1
Lam_2
D
Ca
0
500
1000
1500
2000
2500
Calcite
Canal
Nipp
Stalactite
Lam_1
Lam_2
E
P
0
200
400
600
800
1000
1200
Calcite
Canal
Nipp
Stalactite
Lam_1
Lam_2

781 Figure 5.

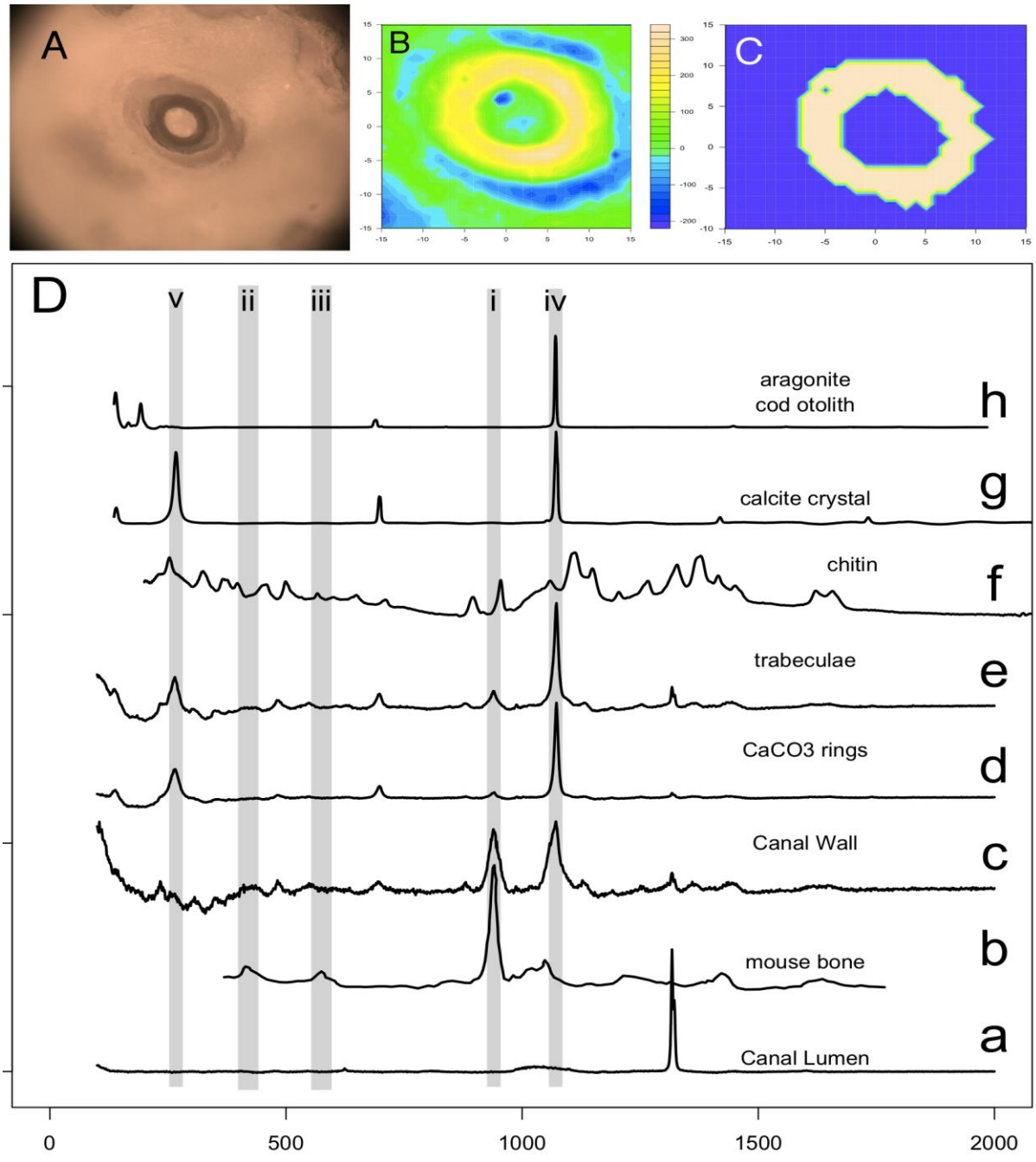
A
B
C
D
v
ii
iii
i
iv
aragonite
cod otolith
h
calcite crystal
g
chitin
f
trabeculae
e
CaCO3 rings
d
Canal Wall
c
mouse bone
b
Canal Lumen
a
0
500
1000
1500
2000

783 Figure 6.

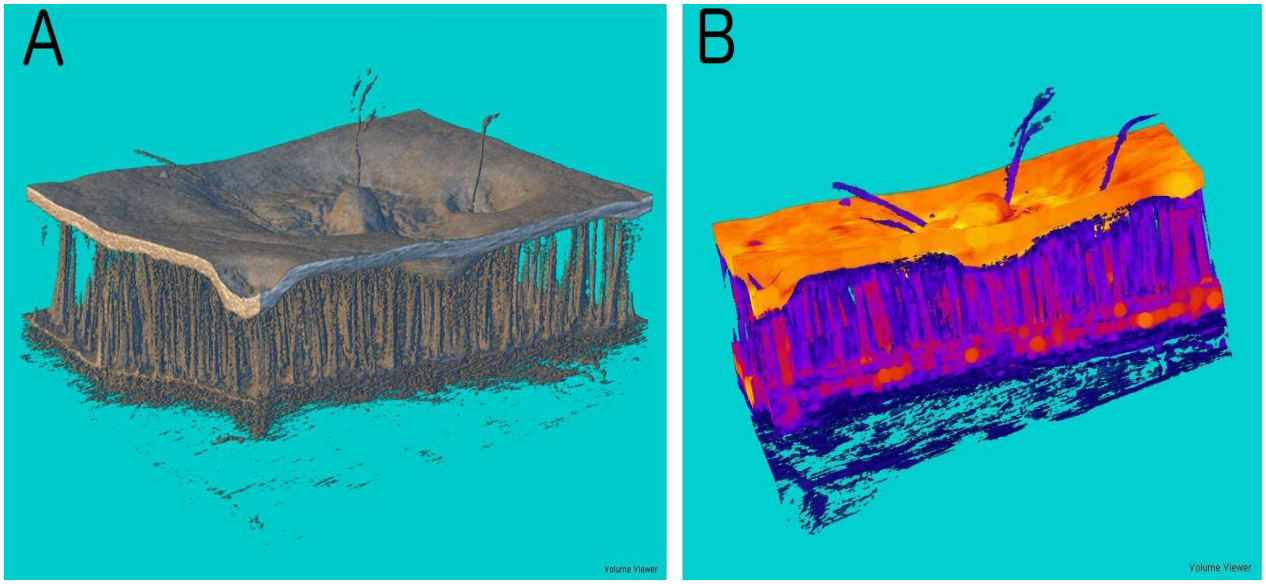

784

785 Figure 7.

786

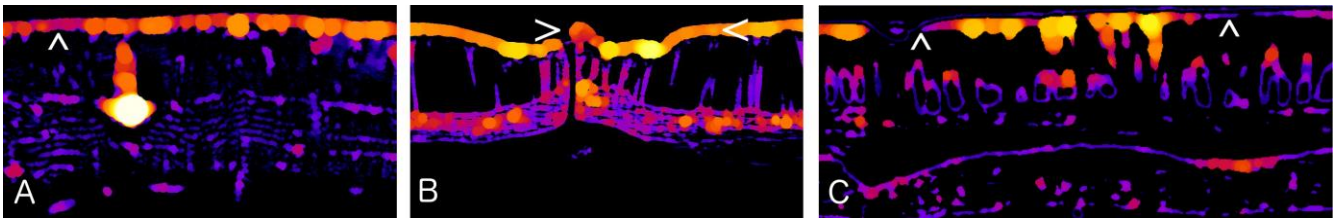

787

788 Figure 8.

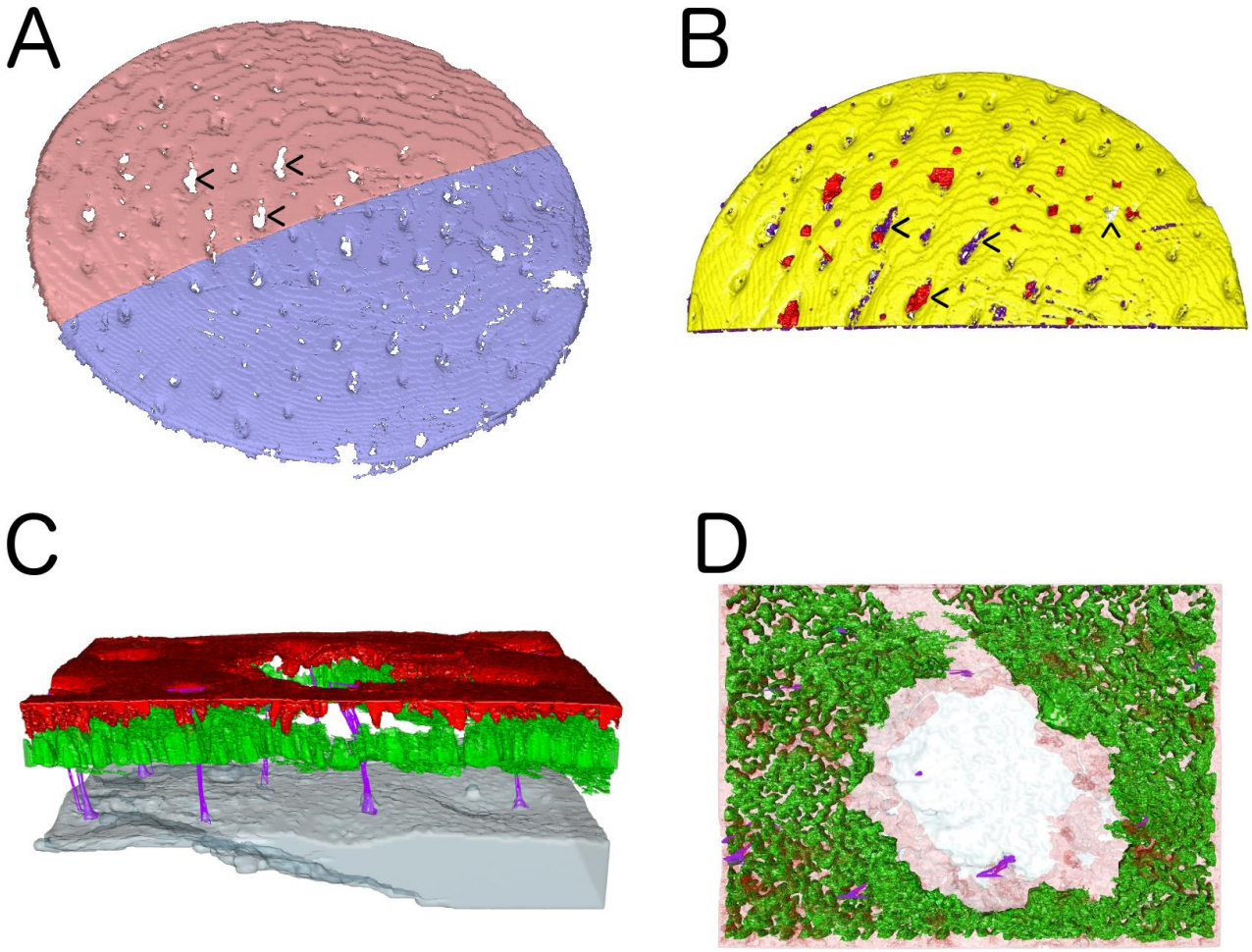

789

790 Figure 9.

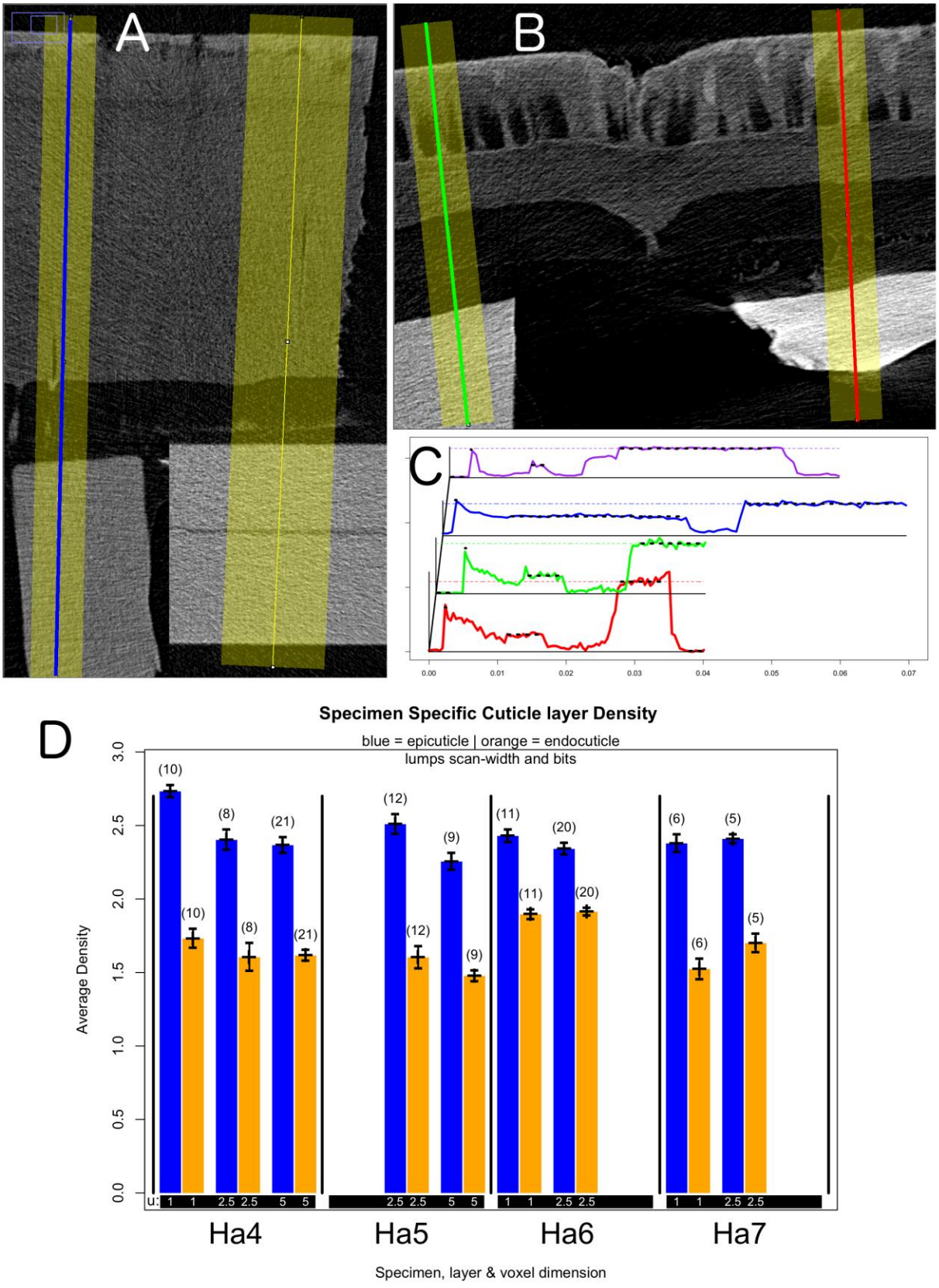
A
B
C
0.00
0.01
0.02
0.03
0.04
0.05
0.06
0.07
D
Specimen Specific Cuticle layer Density
blue = epicuticle | orange = endocuticle
lumps scan-width and bits
Average Density
0.0
0.5
1.0
1.5
2.0
2.5
3.0
u:
1 1 2.5 2.5 5 5
2.5 2.5 5 5
1 1 2.5 2.5
1 1 2.5 2.5
Ha4
Ha5
Ha6
Ha7
Specimen, layer & voxel dimension

792 Figure 10.

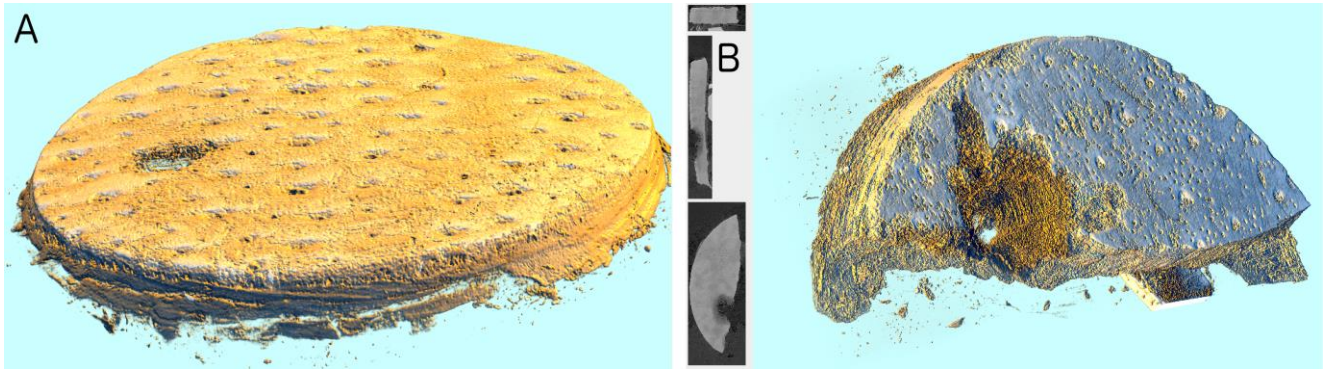

793

794 Figure 11.

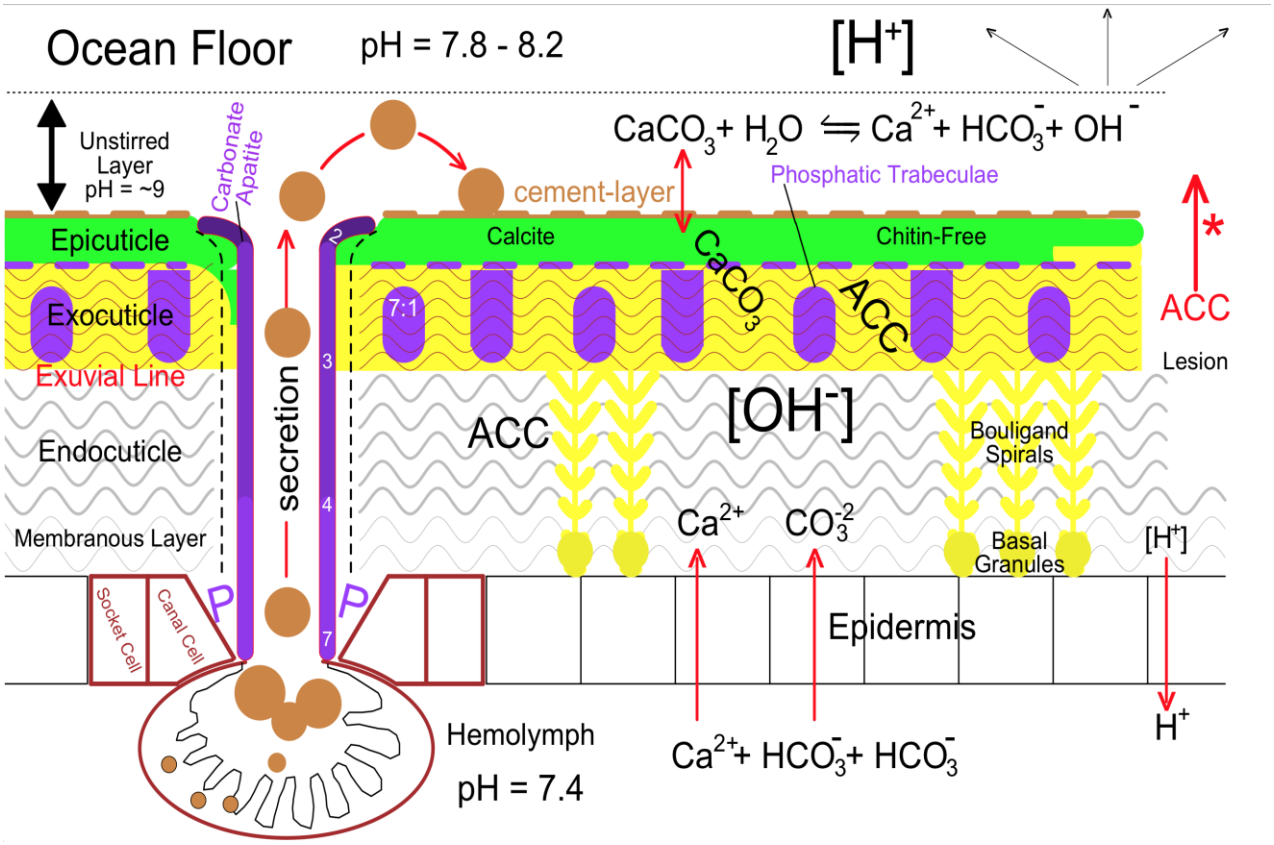

Joseph G. Kunkel, Melissa Rosa, Brian Tarbox, Sabine Hild, Michael J. Jercinovic, Ali N. Bahadur
(2018)

Supplementary Material for **Recognizing Incipient Epizootic Shell Disease Lesions in the Carapace of the American Lobster, *Homarus americanus* H. Milne Edwards 1837.**

Bulletin of Marine Science.

Supplementary Table S1. Raman spectral regions Wavenumber(s) of interest (i – vi) covering PO_4^{3-}, CO_3^{2-}, and chitin and carbohydrate polymers. Critical types mentioned in the text and highlighted in figs 2D and S4D are given lower case Roman numbers.

Critical Type	Bond vibration	Wavenumber(s)	Comments	refs
i	ν1 PO_4^{3-}	957, 961, 962, 966	apatite, hydroxyapatite	[1,2,3]
ii	ν2 PO_4^{3-}	432, 445	[1,3]	[1,3]
iii	ν4 PO_4^{3-}	579, 590, 609		[1,3]
iv	ν1 symmetric CO_3^{2-} stretching, ν1 PO_4^{3-}	1073, 1085	calcite, carbonate apatite	[1,2]
v	ν2 CO_3^{2-} translational lattice vibration	281	calcite (not aragonite)	[2]
	Various amide III (β-sheet, α-helix), Glycine, >CH2, proline-sidechain	1200-1300, 1337	Various amide III	[1,2]
	Protein: CH deformation	1318	canal lumen	[2]
	Various amide II	1544, 1554		[2]
	Various amide I	1634-1690		[1,2,3]
vi	CH stretch (sym), C-H str (Fermi-Resonance) of >CH2 CH stretch (asy), amine	2883, 2935, 2965	chitin, carbohydrate polymers, protein sidechains	[2]
	ν (=C–H) stretch of lipids	3011	lipid	[2]
	O–H and N–H stretching vibrations	3232	-OH and amine stretch	[2]
	O–H stretching vibrations	3350 – 3550	-OH stretch	[2]

1. Mandair and Morris, 2015.
2. Movasaghi et al. 2007.
3. Kozielski et al. 2011.

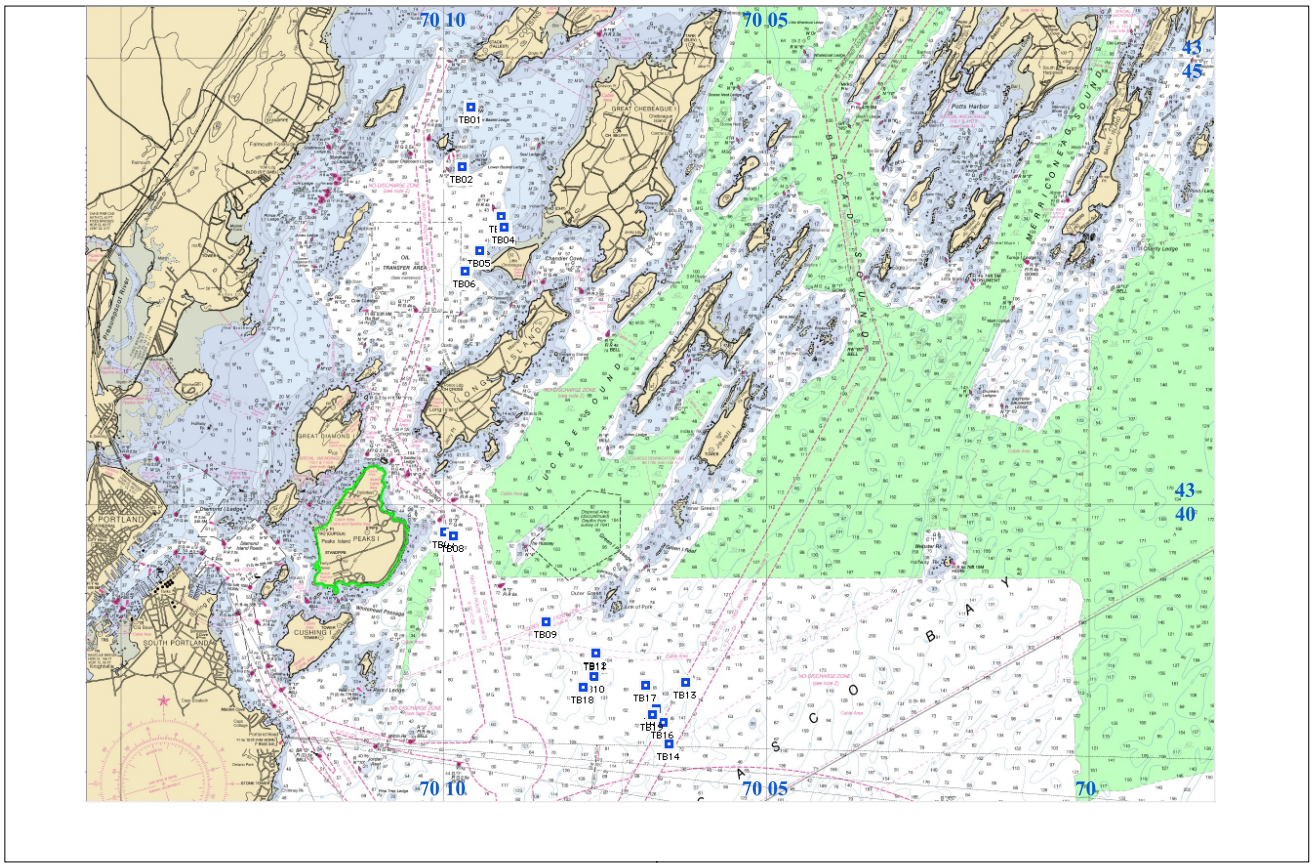

Figure S1. Lobster sampling sites in Casco Bay, Maine. Trap locations. Traps BT01-06 are referred to as Inner Casco Bay. Traps BT09-19 are referred to as Outer Casco Bay.

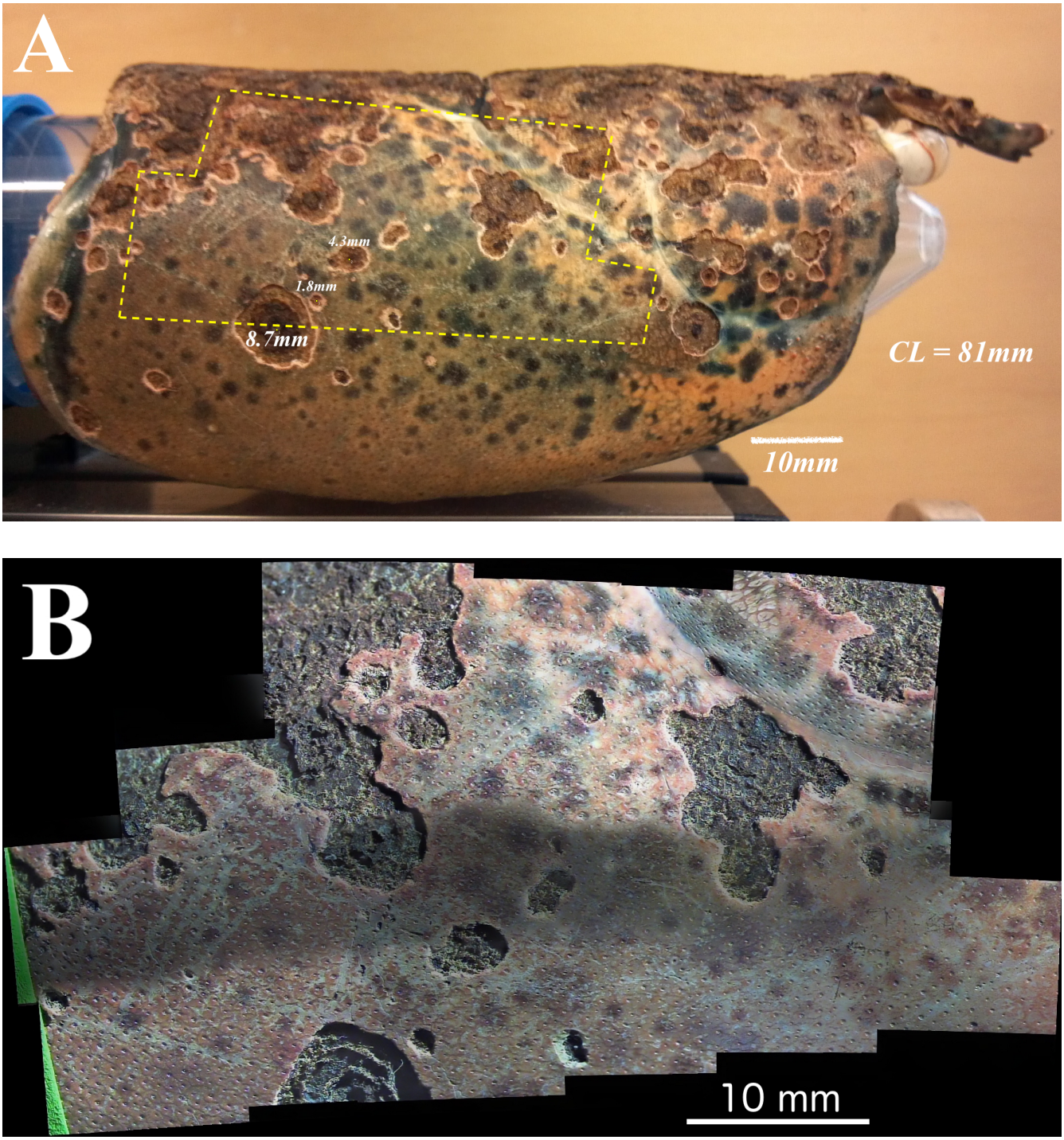

Figure S2. Exemplar ESD shell diseased lobster S6. **A.** Carapace (right half) molted from an advanced ESD infected American lobster. ImageJ calibration from CL = 81 mm allowed the sizes of lesions and the calibration bar to be provided. A yellow dash outlines the area that was the source of the 22 light microscope (LM) images used to create panel B. **B.** Montage of 22 hi-res LM images grabbed from center region of S6-A lobster combined via PhotoSticher with organules and large and small lesions. It is difficult to differentiate the smallest ESD lesions from large high-complexity organules at this level or resolution. The raw PhotoSticher output file is available to judge the visibility of small lesions at URL: http://www.bio.umass.edu/biology/kunkel/LabWiki/images/c/c8/Montage_stereograph100.jpg … to allow evaluation of effectiveness of viewing at this resolution.

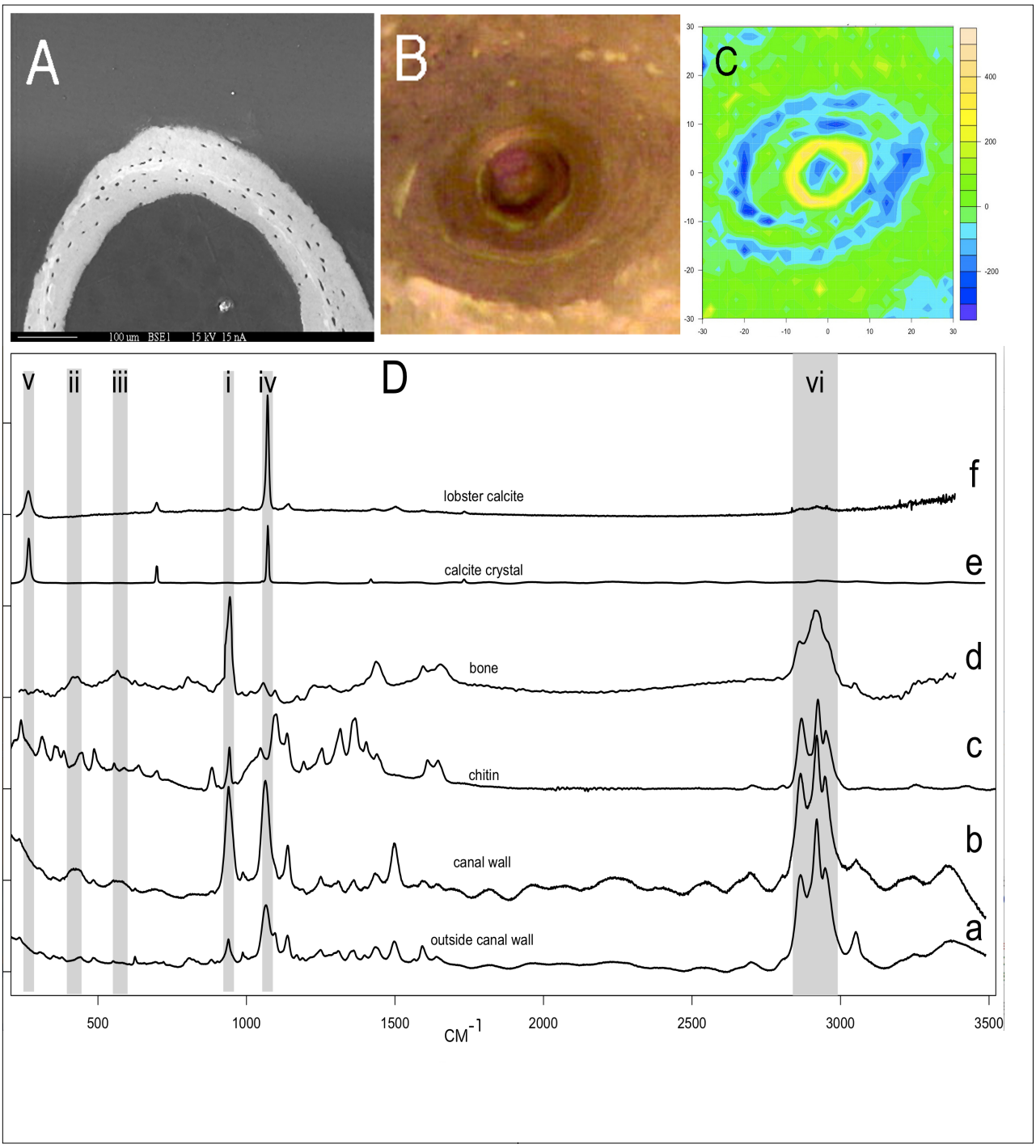

Figure S3. Raman spectra of selected areas of lobster cuticle in tangental polished section including the 2800-3400 μm^{-1} polymer region. A. Neonatal mouse cancelous bone. B. LM image of dermal canal. C. svd V7 contrasting canal wall to other surrounding structure. D. Raman Spectra a-f as intensity vs cm^{-1}: a. Outside canal wall. b. Canal wall. c. alpha-chitin crystal. d. neonatal mouse bone. e. calcite crystal. f. Lobster calcite layer (Thermo Fisher DX). Grey highlighted zones: *i.* v1 PO_4, *ii.* v2 PO_4, *iii.* v3 PO_4 , *iv.* v1 CO_3, *v.* v2 CO_3; *vi.* v3 CO_3.

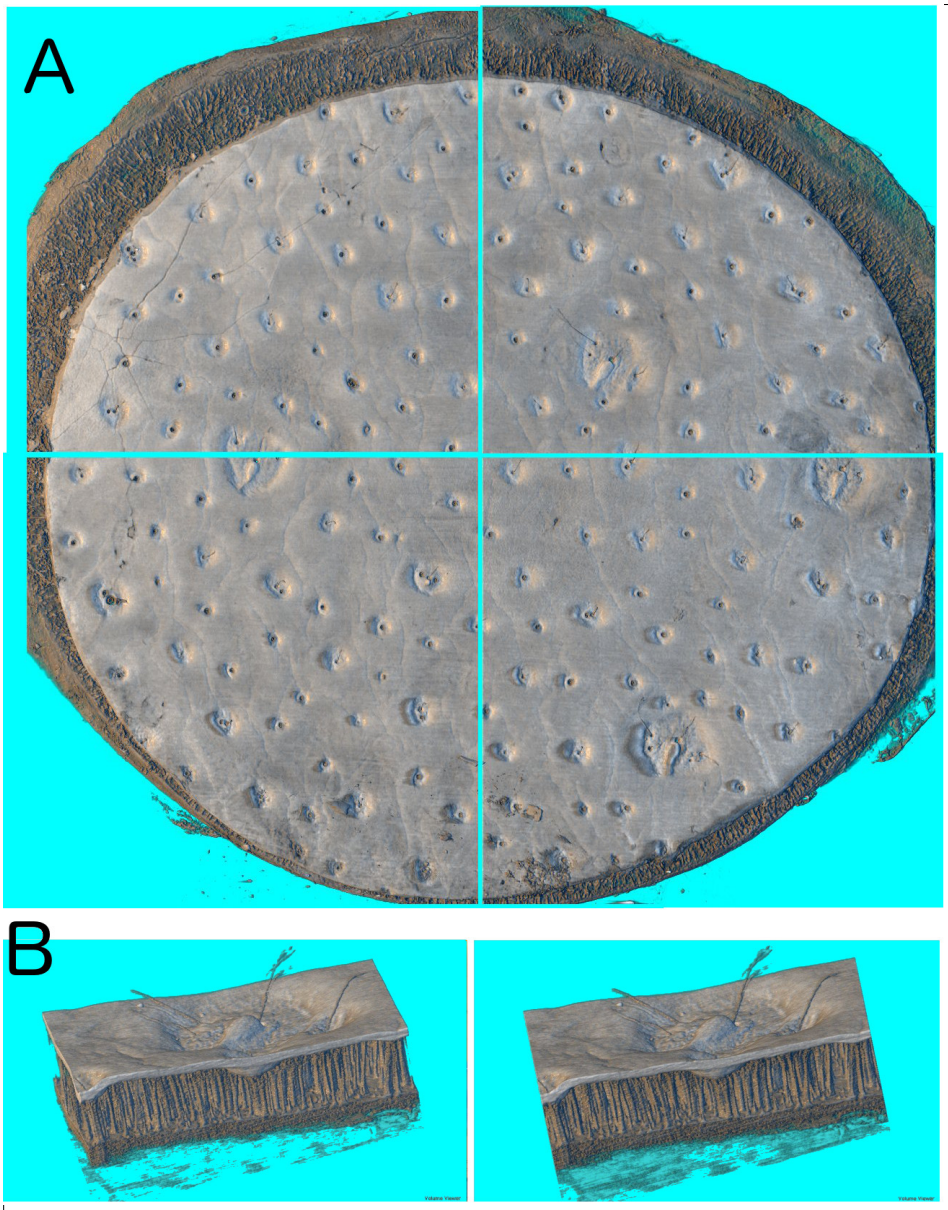

Figure S4. One-week post molt carapace cuticle medallion. **A.** Four sectors of data were analyzed separately using identical protocols in ImageJ VolumeViewer because the full 2.5 µm voxel resolution 6 mm diameter medallion 16 bit data set was too large to be analyzed together. The resultant images were saved and combined with GIMP software. **B.** A ROI of the same medallion scanned at 1 µm voxel resolution showing the organule of Fig. 3 and Fig. 4B as a stereo pair which allows one to see more clearly the organule canal freeze-fixed-secretion streaming in the space above the organule depression onto the epicuticle surface. The stereo pair can be viewed effectively by uploading into a phone browser and viewing with a VR viewer or by cross-eye viewing. Various size choices are offered ... URL:
http://www.bio.umass.edu/biology/kunkel/LabWiki/images/thumb/a/a0/Ha7_1um_b_stereo.jpg

A video of an organule with a bristle is instructive:
http://www.bio.umass.edu/biology/kunkel/LabWiki/images/3/38/Ha7_2.5_crop2A_ThMacrCx0.6.avi

Another video illustrates applying the ImageJ Bone/thickness plugin to Fig. 4C medallion sections:
http://www.bio.umass.edu/biology/kunkel/pub/lobster/3D/AVI/Ha5_2.5_aX300center.avi

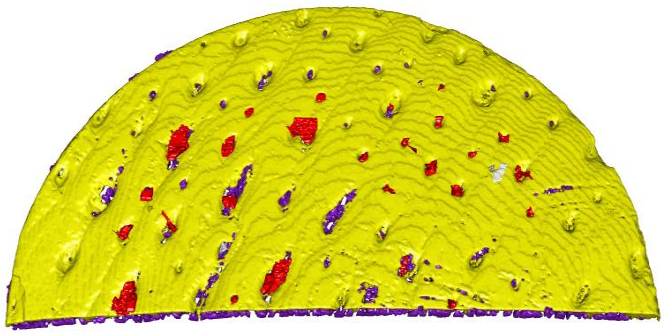

Figure S5. Video of American lobster 6 mm hemi-medallion viewed in (Kunkel et al. 2018) Fig. 8A,B illustrating a potential subclinical ESD lesion. The calcite layer is yellow, the trabeculae are purple and some canals and organule depression contents were characterized as red. A few structures that did not conform to the criteria of calcite, trabeculae, stalactites or canal contents in the epicuticle and exocuticle region were defined as white and one such large such object is seen at about 2 o'clock on the face of this S5 video, URL:

http://www.bio.umass.edu/biology/kunkel/pub/lobster/3D/XRT/Ha5_2.5/16bit/AVI/interp/Ha5_2.5um_16b_semiMedalionA3.avi

This white object was not fully understood and is a potential subclinical ESD lesion residing close to an organule.

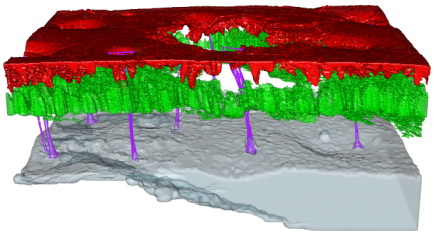

Figure S6. Video of ROI (Kunkel et al. 2018) Figs. 7A, 8C,D and 10A, a 50 µm ESD lesion, based on 1 µm resolution µCT data from American lobster medallion Ha4.

http://www.bio.umass.edu/biology/kunkel/pub/lobster/3D/XRT/Ha4_1um/AVI/interp/Ha4_1um_16b_transp_0-325_237.avi

REFERENCES

1. Mandair GS, Morris MD. (2015). Contributions of Raman spectroscopy to the understanding of bone strength. BoneKEy Reports 4(620):1-8. https://doi.org/10.1038/bonekey.2014.115

2. Movasaghi Z, Rehman S, Rehman IU. (2007). Raman Spectroscopy of Biological Tissues. Applied Spectroscopy Reviews 42(5): 493-541. http://dx.doi.org/10.1080/05704920701551530

3. Kozielski M, Buchwald T, Szybowicz M, Błaszczak Z, Piotrowski A, Ciesielczyk B. (2011). Determination of composition and structure of spongy bone tissue in human head of femur by Raman spectral mapping. Journal of Materials Science: Materials in Medicine 22(7): 1653–1661. https://doi.org/10.1007/s10856-011-4353-0